Chapter 2
The Modelling of Fibre Lasers for Mid-Infrared Wavelengths

L. Sojka, T.M. Benson, D. Furniss, Z. Tang, H. Sakr, A.B. Seddon and S. Sujecki

Abstract This chapter describes numerical investigations of some of the possibilities for obtaining mid-infrared laser action in rare earth doped chalcogenide glass fibres, starting from some basic laser physics and progressing through the development of numerical fibre laser models and the experimental techniques for extracting modelling parameters.

2.1 Introduction to Mid-Infrared Fibre Lasers

2.1.1 Mid-Infrared Lasers; Technology Drivers and Potential Applications

Mid-infrared light sources are one of the most quickly developing subjects in the photonic area in recent years. The reason for this is that they can find many applications, for example in:

- remote sensing; many gases e.g. CO_2, N_2O, CO have an absorption band in the mid-infrared region [1–3].
- medicine; many human tissues have absorption in the mid-infrared region so they respond better to treatment with a laser that works in the mid-infrared region [1, 4] and
- security and military applications; including the sensing of toxic gases, the detection of explosives and infrared counter-measurements [1].

In order to find application in these areas sources should offer: compact dimensions, robust construction, affordable price, high efficiency, high output power, vast tuning range and good output beam quality. One of the types of lasers that can combine all these features is fibre lasers.

L. Sojka · T.M. Benson (✉) · D. Furniss · Z. Tang · H. Sakr · A.B. Seddon · S. Sujecki
George Green Institute for Electromagnetics Research, University of Nottingham, University Park, Nottingham NG7 2RD, UK
e-mail: trevor.benson@nottingham.ac.uk

A. Agrawal et al. (eds.), *Recent Trends in Computational Photonics*,
Springer Series in Optical Sciences 204, DOI 10.1007/978-3-319-55438-9_2

2.1.2 Overview of Mid-Infrared Fibre Lasers

Over the past decades silica fibre has revolutionised optical technology. Using a silica-based erbium doped fibre amplifier (EDFA) the signal in an optical network can be amplified and transmitted over several hundreds of kilometres directly in the optical domain. However, the working wavelength bands of commercially available rare earth (RE) doped fibre lasers are from 0.5–3 μm, with a significant spectral gap beyond 3.5 μm. One problem with obtaining higher wavelengths is connected with the host glass material. Lanthanides possess many transitions in the mid-infrared range. However these transitions can be quenched by the host material [5–11]. For example, the most popular material used to elaborate fibre lasers is silica. However the phonon energy of silica is 1100 cm^{-1} and this is the reason why wavelengths above 2 μm are strongly quenched in this material. In order to construct a mid-infrared fibre laser a suitable host material, with low phonon energy, has to be manufactured. Lower phonon energy host glasses are required to reduce the multiphonon relaxation rates for mid-infrared transitions. At the time of writing the fibre laser with the longest continuous emission wavelength, at 3.9 μm in a holmium (III) doped ZBLAN (ZrF_4-BaF_2-LaF_3-AlF_3-NaF) glass fibre, was achieved by a group at the University of Braunschweig [8]. However this result was only demonstrated for a fibre cooled down to 77 K. Room temperature laser action was not detected [12, 13]. Recently, a Er:ZBLAN continuous wave laser operating at 3.5 μm with high efficiency was reported. The slope efficiency of this laser showed an order of magnitude improvement over previous work. This was done by using a novel double pumping scheme at 1.973 and 0.985 μm, respectively. 250 mW of output power at 3.5 μm was produced by this laser for input powers around 2150 mW for 1.973 μm and 200 mW for 0.985 μm [14]. In 2015 Berrou et al. [15] reported the mid-infrared lasing at 3.9 μm from Ho^{3+} in bulk In F_3 glass. The laser system had a slope efficiency of 1.6%. However, this laser only operates in pulse regime due to pulse pumping at 0.889 μm [15]. Chalcogenide glasses offer significant advantages in the mid-infrared wavelength region. These advantages include a low phonon energy, from 400 cm^{-1} up to 230 cm^{-1} depending on the glass composition. Consequently, chalcogenide glasses present low non-radiative decay rates and wide infrared transparency. These glasses also have a high refractive index which results in higher absorption and emission cross-sections in RE doped glasses. No laser action from rare earth doped optical fibres at a wavelength beyond 4 μm has been reported up to date. Therefore this chapter presents the recent research activities of the authors towards achieving the first mid-infrared fibre laser operating above 4 μm [15].

The chapter is divided into seven sections. After this introduction, Sect. 2.2 describes the physics underpinning the operation of a fibre laser. The current state-of-the-art in mid-infrared optical fibre materials is presented in Sect. 2.3. In Sect. 2.4, the experimental procedures that are used to obtain the spectroscopic parameters for modelling lanthanide doped fibre lasers are described. The fibre laser numerical models are discussed in Sect. 2.5. Numerical studies towards mid-infrared laser action in rare earth doped chalcogenide glass with Dy^{3+}, Pr^{3+} or Tb^{3+} are presented in Sect. 2.6. Finally, some conclusions are drawn in Sect. 2.7.

2.2 The Physics of Fibre Laser Systems

This section provides the Reader with necessary information for understanding the physics underpinning the operation of a fibre laser.

2.2.1 Light-Matter Interactions in Gain Medium

In order to describe the physical process in a gain medium we examine an atomic two level system as shown schematically in Fig. 2.1. In this configuration there are two levels corresponding to energies E_1 and E_2 such that $E_1 < E_2$ [16–22]. N_1 and N_2 define the number of atoms per unit volume in each of the two states, respectively. The atom population in thermal equilibrium is expressed by the Boltzmann distribution [16–19].

$$\frac{N_2}{N_1} = \exp\left(-\frac{E_2 - E_1}{k_B T}\right) \tag{2.1}$$

where k_B is Boltzmann's constant, and T is the absolute temperature (in Kelvin).

The first process that will be considered is absorption. The atom in the ground state can make an upward transition to the upper state 2 by absorbing a photon of energy equal to $E_{21} = E_2 - E_1$ (see Fig. 2.1). The absorption depends on the photon energy; it needs to match the energy difference between the levels 1 and 2. Absorption is an induced process. The probability of absorption per unit time can be given by [16–19]:

$$W_{12}^a = B_{12} \times \rho(\nu) \tag{2.2}$$

where B_{12} is an Einstein coefficient with dimensions $m^3/(J \times s)$ and $\rho(\nu)$ is the spectral density, defined as the radiated energy density per unit frequency interval per unit volume [16–22]. $\rho(\nu)$ is related to the intensity I and photon flux (ϕ) using [16–19]:

$$\rho(\nu) = \frac{n}{c} \times I(\nu) = \frac{n \times h \times \nu}{c} \times \phi(\nu) = n \times \hbar \times \omega \times \phi(\nu) \tag{2.3}$$

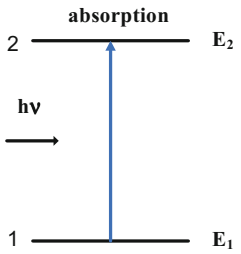

Fig. 2.1 Schematic representation of absorption in a two-level system

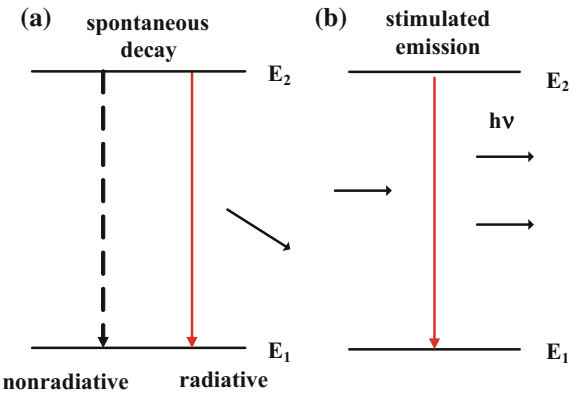

Fig. 2.2 Schematic representation of spontaneous emission (**a**) and stimulated emission **b** in a two-level system. The *dashed line* indicates nonradiative decay

where $\phi = \frac{I}{h\nu}$ is the photon flux defined as the number of photons per area unit area per unit time, I is the optical intensity defined as the power per unit area, n is the refractive index of the medium, c is the speed of light in vacuum, h is Planck's, constant ν is frequency of the wave, $\omega = 2\pi\nu$ is angular frequency and $\hbar = \frac{h}{2\pi}$ is the reduced Planck constant.

An atom in a higher energy state 2 can relax to the lower energy state by emitting a photon. This phenomenon is called spontaneous emission (see Fig. 2.2a). The probability per second of spontaneous emission occurring is defined by another Einstein coefficient, A_{21}. The probability of spontaneous emission, also known as the spontaneous emission rate, can be written as

$$W_{21}^{spe} = A_{21} \tag{2.4}$$

where A_{21} is a rate constant with dimension s^{-1}.

The atom can also spontaneously decay from E_2 to E_1 in a nonradiative manner where no photon is emitted. This process can be due to the interaction between the atoms or a vibration of the host material (see also Sect. 2.2.4).

Another induced process is stimulated emission also known as the emission rate. In stimulated emission a photon forces the atom to go from level 2 into 1 by emitting another photon with the same phase and in the same direction as the initial photon (see Fig. 2.2b). Based on this process amplification in an active media can be achieved. The probability of stimulated emission can be written as:

$$W_{21}^{se} = B_{21} \times \rho(\nu) \tag{2.5}$$

where B_{21} is another Einstein coefficient with dimensions $m^3/(J \times s)$ and $\rho(\nu)$ is the spectral density.

Taking into account all the processes described above, the rate equation for the two-level system is described as [16–19]:

$$\frac{dN_2}{dt} = N_1 \times B_{12} \times \rho(\nu) - N_2 \times B_{21} \times \rho(\nu) - N_2 \times A_{21} \tag{2.6}$$

The Einstein coefficients are related as follows [16–19]:

$$B_{21} = B_{12} \tag{2.7}$$

and

$$A_{21} = \frac{8 \cdot \pi \cdot h \cdot \nu}{c^3} \times B_{21} \tag{2.8}$$

The equations indicate that absorption, stimulated emission and spontaneous emission are strongly related. The relations established in this subsection will be further used in Sect. 2.2.6 and in Sect. 2.5.

2.2.2 Cross−Section

In simple terms, the absorption cross-section defines the effective area over which the atom can absorb a passing photon. The absorption cross-section depends $\sigma_a(\nu)$ on the wavelength of the light and is expressed in units of m^2. The $\sigma_a(\nu)$ multiplied by N (number density, for example (ions/m^3) can be termed as an absorption coefficient $\alpha(\nu) = \sigma_a(\nu) \times N$ [16–19]. Hence, the absorption cross-section can be extracted from absorption measurements.

Emission cross-section describes the likelihood of releasing energy in the form of a photon from an atom in an excited state. Similar to the case of $\sigma_a(\nu)$, the emission cross-section $\sigma_e(\nu)$ also depends on wavelength. The emission cross-section can be extracted from an experimentally measured photoluminescence spectral shape using the Fuchtbauer–Ladenburg equation [16–19]. In order to obtain a reliable result, the emission spectrum cannot be affected by re-absorption or overlap of different fluorescent transitions. Further information about the experimental extraction of absorption and emission cross-sections is given in Sect. 2.4.

2.2.3 Lifetime

The fluorescence lifetime describes the probability per second that an atom in the upper level transits to the lower state. In basic cases the spontaneous emission intensity from an upper level is presented as an exponential decay with time. The decay can

be due to radiative and nonradiative processes. The total lifetime τ_T can be described by following equation [16–19]:

$$\frac{1}{\tau_T} = A_R + A_{NR} = \frac{1}{\tau_R} + \frac{1}{\tau_{NR}} \tag{2.9}$$

where τ_T is the total luminescence lifetime, A_R and A_{NR} are the radiative and nonradiative rates respectively, and τ_R and τ_{NR} are the radiative and nonradiative lifetimes. The radiative lifetime can be calculated from Judd–Ofelt theory [18, 19]. The nonradiative lifetime can be determined experimentally by measuring the total lifetime from a laser transition and comparing this value with the radiative lifetime derived from Judd–Ofelt theory. The nonradiative process is an undesirable phenomenon as far as laser action is concerned because energy from this process is wasted as heat. The nonradiative lifetime depends strongly on the glass composition and the vibration coupling between host and rare earth atoms [18–20].The quantum efficiency η is defined as the ratio of atoms that decay radiatively to the total decay rate A_T. The quantum efficiency can be expressed using the following equation [18–20]:

$$\eta = \frac{A_R}{A_T} = \frac{A_R}{A_R + A_{NR}} \tag{2.10}$$

The quality of the host material is often evaluated based on quantum efficiency. A high quantum efficiency indicates that the radiative process dominates over nonradiative ones [16–20].

2.2.4 Nonradiative Lifetimes

A situation commonly encountered is that the experimentally measured fluorescence lifetime is smaller than the calculated one. As noted in the previous subsection, this can be explained in the context of a nonradiative emission occurring simultaneously with the radiative transition. The probability of nonradiative processes A_{NR}, can be described using the following equation [1, 18–20]:

$$A_{NR} = B_{gh} \times (n(T) + 1)^p \times \exp(-\alpha_{gh} \times \Delta E) \tag{2.11}$$

where p is the number of phonons required to bridge the gap ΔE:

$$p = \frac{\Delta E}{\hbar\omega} \tag{2.12}$$

$\hbar\omega$ is the energy of the phonon. Parameters B_{gh} and α_{gh} in (2.11) describe the host material, n(T) is the Bose-Einstein number, which describes the phonon population as a function of temperature:

$$n(T) = \frac{1}{exp(\frac{\hbar\omega}{kT}) - 1} \tag{2.13}$$

The nonradiative transition probability is the same as the multiphonon relaxation rate A_{NR}, when ion-ion interactions are neglected. The multiphonon relaxation rate increases exponentially with decreasing energy gap ΔE that needs to be bridged by the particular phonons [16–22]. The phonon energy depends on the vibrational frequency of the anion-cation bonds of the glass [1, 18–20]. Usually, glasses comprised of large anions and larger cations show low phonon energy, and consequently high transparency in the mid-infrared region [1, 18–20]. Therefore glasses with heavier ions in the lattice have a lower phonon energy and according to formula (2.11), a slower multiphonon relaxation rate. Experimentally, the phonon energy $\hbar\omega$ may be obtained using Raman Spectroscopy [1].

The constants α_{gh} and B_{gh} in (2.11) are experimentally determined parameters which are constant for a given host glass. They are derived from fitting (2.11) to the experimental A_{NR} against energy gap (ΔE) data. The A_{NR} is determinated using $A_{NR} = A_T - A_R$. The chalcogenide glasses have the lowest phonon energy amongst optical glasses. Consequently, they have the lowest nonradiative rates in the 3–6 μm region. Hence, they are potentially the best host materials for mid-infrared fibre lasers.

2.2.5 Branching Ratio

The branching ratio defines the relative intensities of the transitions from an excited level (i) to all terminated levels. In other words it is the amount of spontaneous radiation from the actual laser transition to all lower levels. The sum of branching ratio for all possible transitions must be unity i.e. $\sum_j \beta_{ij} = 1$.

The branching ratio is calculated using following equation [16–19]:

$$\beta_{ij} = \frac{A_{ij}}{\sum_j A_{ij}} = A_{ij} \times \tau \tag{2.14}$$

where β_{ij} is the branching ratio, A_{ij} is the radiative rate for transition ij and τ is the total luminescence lifetime. Generally the branching ratios are determined using Judd–Ofelt theory [18–22].

2.2.6 Gain in Active Media

Gain in an active medium depends on the balance between the two induced processes of stimulated emission and absorption. The amplification process is illustrated

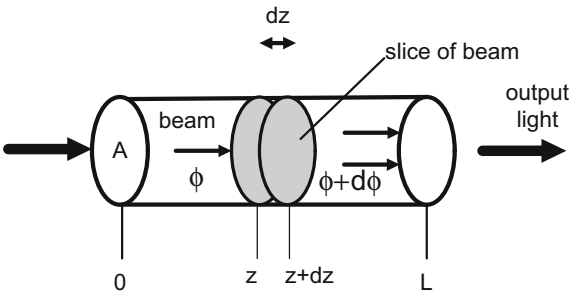

Fig. 2.3 Photon flux amplification in a gain medium [16–19]

schematically in Fig. 2.3. The number of photons added per unit volume per second can be described using [16–22]:

$$\frac{photons_{added}}{(volume)(time)} = \frac{d\phi}{dz} = N_2 W_{21} - N_1 W_{12} = \Delta N W \tag{2.15}$$

where ϕ is the photon flux, (see Sect. 2.2.1), N_2 and N_1 are the population densities of upper and lower laser levels, $W_{21} = \sigma_e(\lambda) \times \phi$ and $W_{12} = \sigma_a(\lambda) \times \phi$ are probability densities that an atom emits or absorbs a photon respectively, where σ_e and σ_a are emission and absorption cross-sections as described in Sect. 2.2.2. The probability densities have been introduced in Sect. 2.2.1. The (2.15) can be expressed in the form:

$$\frac{d\phi}{dz} = (N_2\sigma_e(\lambda) - N_1\sigma_a(\lambda)) \times \phi \tag{2.16}$$

The gain coefficient $\gamma(\lambda)$ can be defined as [16–19]:

$$\gamma(\lambda) = N_2\sigma_e(\lambda) - N_1\sigma_a(\lambda) \tag{2.17}$$

such that

$$\frac{d\phi}{dz} = \gamma(\lambda) \times \phi \tag{2.18}$$

The gain in an active medium depends on the population densities N_2 and N_1 and the absorption and emission cross-sections. Equation (2.17) shows that when $N_2\sigma_e > N_1\sigma_a$ we have amplification. To achieve amplification this "population inversion" condition must be satisfied.

In the case of $N_2\sigma_e < N_1\sigma_a$ we have attenuation, the photon-flux density decreases on propagation. If $N_2 - N_1 = 0$, the medium is transparent. Considering equation (2.17) it can be concluded that knowledge of the emission and absorption cross-sections is very important in amplifier and laser design [1, 16–22].

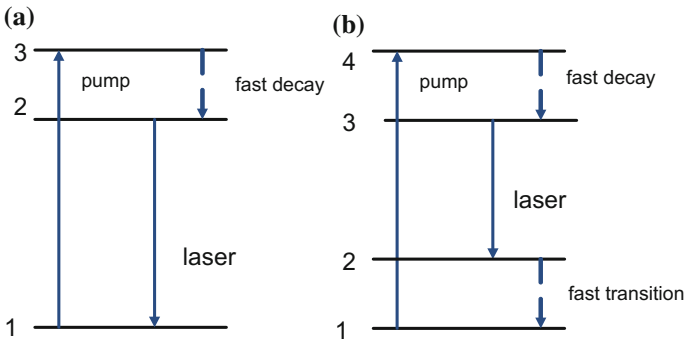

Fig. 2.4 Simplified diagram of the energy levels in a three level laser system (**a**) and four level system (**b**)

2.2.7 Laser Systems

In the previous section the gain in an active material was explained for a two level system. However in general, lasers operate in three or four level systems. A simplified diagram of the energy levels for a three level system is depicted in Fig. 2.4a. In this system the atoms are excited from the ground state (level 1) into level 3 using a pump. They rapidly decay into the long lived level 2 emitting a phonon. The long lifetime of level 2 allows a population inversion to occur between levels 2 and 1; amplification of a signal beam can thus occur due to stimulated emission. The disadvantage of this configuration is that in order to achieve population inversion more than half of the atoms need to be excited to the upper laser level (2). This requires that high pump energy is needed i.e. the associated laser threshold is relatively high. The most popular three level laser systems are erbium doped solid state lasers operating at 1.55 μm [16–22].

A simplified diagram of a four level laser system is shown in Fig. 2.4b. In this laser system the atoms are excited from the ground state (level 1) to level 4 using a pump. From level 4 they rapidly decay into level 3 emitting a phonon. A long lifetime of the level 3 combined with a short lifetime of the level 2 allows population inversion to build up in level 3 relative to level 2. Population inversion can be readily achieved in this system, because the laser action is between levels 3 and 2 and not with the respect to the ground state. Four level systems thus have low thresholds [16–22].

2.2.8 Laser Theory

In Sect. 2.2.6 it was shown that light can be amplified by a stimulated emission process. In order to make a laser, positive feedback needs to be added to the system. This can be done by placing the active medium into a cavity consisting, for example,

of two high reflectance dichroic mirrors or fibre Bragg gratings (FBG). A dichroic mirror is a mirror with significantly different reflection or transmission properties at two different wavelengths. For example in a laser cavity the dichroic mirror should have high transmission for the pump wavelength in order to pass the pump energy into gain medium. On the other hand it should be highly reflective for the laser wavelength in order to provide a high degree of feedback [16–19]. A fibre Bragg grating (FBG) can also provide wavelength dependent reflectivity controlled by forming a periodic variation in the refractive index of the fibre core. The dichroic mirrors or FBGs, at each end of the cavity, reflect the light backwards and forwards within the cavity end; on every round trip, more and more photons are generated.

The dichroic mirrors or FBGs should provide sufficient feedback to ensure laser action. The laser cavity can be also formed by Fresnel reflection from the end facets of the gain medium and air [16–22]. There are two requirements for laser action: a gain condition, and a phase condition. The gain condition states that in order to achieve the laser action the round trip gain must be greater than the cavity loss [16–22]. The phase condition states that the phase shift in a single round trip must be an integer multiple of 2π to ensure that the phase of the signal feedback at the input matches the phase of the original input [16–22].

Rare earth ions are key materials for development of fibre laser, therefore in the next subsection the physical properties of rare earth ions are briefly described.

2.2.9 Rare Earth Doping

The rare earths (or lanthanides) form the lanthanide series of 14 similar elements with atomic number in the range from 58 to 71 in the Periodic Table.

The rare earths have the following electronic configuration $1s^2 2s^2 2p^6 4s^2 3d^{10} 4p^6 5s^2 4d^{10} 5p^6 6s^2 4f^x (5d^1)^2$, where x varies from 1 to 14 across the series. When these elements are doped in glass fibres, they become triply ionised. Rare earth ions are important in the development of lasers since the f electrons involved in these optical phenomena are not greatly influenced by the crystal field of the surrounding host material. The 4f shell is the only shell that is not complete. However, the other shells are fully occupied. Therefore 4f electrons are shielded by the outer 5s and 5p shells. This results in 4f$\longrightarrow$4f optical transitions which are comparatively sharp and are only weakly sensitive to the host material [16–19]. The energy level of each ion can be described using the Russell-Saunders notation $2S + 1L_J$,where S is the total spin quantum number, L is the orbital angular momentum quantum number, J is total angular momentum quantum number, with J = L + S and 2J + 1 is the degeneration of the level. More complete information about the identification of particular transition in rare earth ions can be found in the literature [16–22].

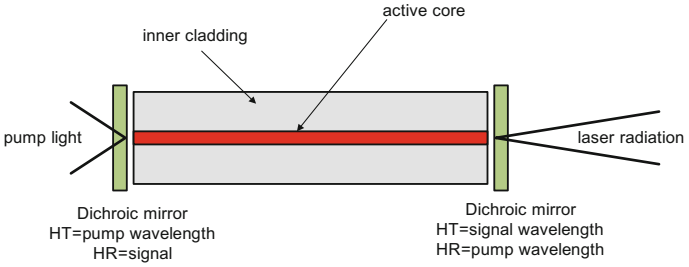

Fig. 2.5 Schematic diagram of a glass fibre laser

2.2.10 Fibre Lasers

The laser concept has been introduced in previous Sects. 2.2.6–2.2.8 of this chapter. This section focuses on the principle of operation of a fibre laser. A simplified diagram of a fibre laser is shown in Fig. 2.5. It is based on a rare earth ion doped core-clad fibre. The doped core diameter is typically of the order of several microns or tens of microns depending on the application. The pump and laser radiation are guided in the core region of the fibre. The laser cavity is constructed using butt coupled dielectric dichroic mirrors or inscribed in-fibre structure fibre Bragg gratings. A fibre laser structure is very robust and simple in comparison with solid state or gas lasers. All elements can be integrated and do not require alignment or maintaining. This is one of the main reasons why fibre lasers have found many applications in industry [16–22].

Fibre lasers can be characterised by [16–48]:

- A fully fibrerised laser cavity; this eliminates problems with optical alignment
- High optical gain
- Good quality of output beam, a fibre laser can work in a single mode regime producing a beam close to diffraction limits
- High efficiency, for example more than 70% for ytterbium doped silica fibre lasers
- A low threshold achieved through the use of a small core fibre. The damage threshold power of a fibre can be controlled using a large mode area fibre
- Broad tuning range
- Compact size; the fibre laser can be bent or coiled
- Low cost of production, from one doped glass preform hundreds of metres of doped fibre can be produced

2.3 Materials and Dopants

2.3.1 Short Review of Mid-Infrared Optical Fibre Materials

In order to access the mid-infrared spectral range a material with a low phonon energy is needed. Materials with low phonon energy have two desirable properties. First they

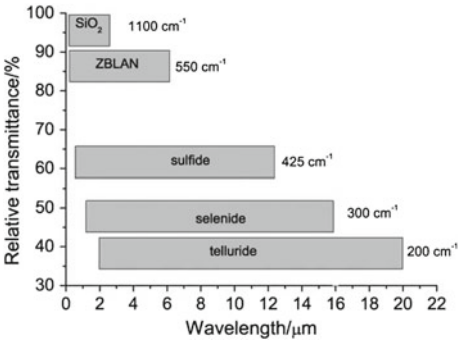

Fig. 2.6 Transmission wavelengths range for silica, ZBLAN and chalcogenide glasses [49, 50]

Table 2.1 Typical vibrational energies of bonds between ions in various glasses [1, 5–7, 18–20, 50–52]

Glasses		Multiphonon energy (cm^{-1})
Oxides	Borate	1400
	Phosphate	1200
	Silicate	1100
	Germanate	900
	Tellurite	700
Non-oxides	Fluorides (e.g. ZBLAN)	550
	Sulfides	425
	Selenide	300
	Selenide/Telluride	230

are transparent in the mid-infrared wavelength region (2 up to 20 μm). Figure 2.6 presents the transmission ranges for silica, fluorides (i.e. ZBLAN) and chalcogenide glasses, respectively. Chalcogenide glasses demonstrate good mid infrared transmission. Small bulk sulfide glasses of a few mms path length transmit light typically up to wavelength of 10 μm selenide glasses up to about 16 and 20 μm for some telluride glass composition (see Fig. 2.6) [49]. Secondly the multiphonon absorption rate of rare earth ions is greatly reduced in these hosts. In Table 2.1 the phonon energies for various glasses are presented. The definition of phonon energy has been described in Sect. 2.2.4. Only a limited number of glasses have suitably low phonon energy in order to achieve emission at wavelengths beyond 3.5 μm [1, 5–7, 18–20].

The chalcogenide glasses are good candidates for use as the host material for a mid-infrared laser. The first reason for this can be seen from Table 2.1; the chalcogenide glasses have the lowest multiphonon energy when compared with other materials used to produce fibre lasers (fluorides, silicate see Table 2.1) [1, 5–7, 18–20, 50–52]. Chalcogenide glasses are based on the chalcogen elements sulfur, selenium and tellurium, but not oxygen, from Group 16 of the new Periodic Table, along with elements usually from the 14 and 15 Groups to form a stable glass. These glasses are chemically and mechanically durable [5–7, 49, 50]. It is difficult to fabricate high

purity chalcogenide glasses with low losses, but this problem can be overcome by using special purification techniques [53–55]. The second reason that is chalcogenide glass exhibits excellent resistance to moisture corrosion in comparison to fluoride glasses.

2.3.2 *Overview of Mid-Infrared Emission from Chalcogenide Glasses and Fibres Doped with Pr^{3+}, Dy^{3+}, Tb^{3+}*

In the literature we can find several publications about rare earth doped chalcogenide glasses [5–7, 53–73]. Rare earth doped chalcogenide glass has all the necessary parameters to construct an efficient laser that is: high emission and absorption cross-sections, long lifetimes, and high quantum efficiencies [5–7, 53–73]. The mid-infrared transitions are efficient in chalcogenide glass due to the low phonon energy of the host. Rare earth energy level diagrams show possible mid-infrared radiative transitions in chalcogenide glasses (see Fig. 2.7). It can be seen that almost all rare earth ions possess transitions in the mid-infrared range (except Yb^{3+} and Gd^{3+}). In Fig. 2.7 the mid-infrared emissions reported in the literature are indicated using arrows. However, despite this promise, no successful realisation of a chalcogenide glass based mid-infrared fibre laser has been presented in the literature. Only laser action in a rare earth doped chalcogenide glass fibre at 1080 nm was reported. This was achieved for a 22 mm long gallium lanthanum sulphide glass fibre; but such fibre required a lot of oxide to be added (to avoid devitrification) thus lowering their phonon energy and lasing wavelength achievable [6]. The fibre had a 14 μm core

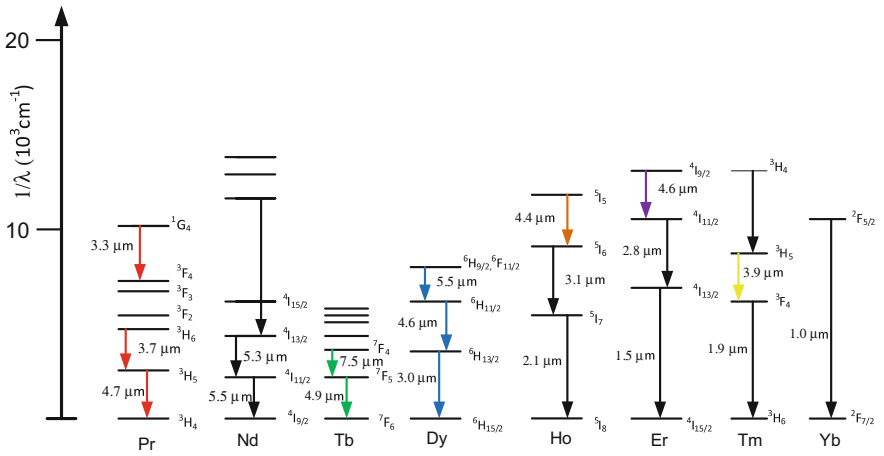

Fig. 2.7 Rare earth diagram adapted from Diekie [74], with the arrows indicating mid-infrared transitions in rare earth doped chalcogenide glasses reported in [57–73]. The notation that has been used to label the transition in rare earth ions is briefly explained in Sect. 2.2.9 [74]

Table 2.2 Characteristics of rare earth doped chalcogenide glasses with emission beyond 3.5 μm. The table is based on recent results presented in the world literature [57–73]

Dopants	Host glass	Pump λ(μm)	Emission λ(μm)	Transition	Reference
Pr^{3+}	$Ga_5Ge_{25}Sb_{10}Se_{60}$	2.0	4.8	$^3F_2, ^3H_6 - ^3H_5 + ^3H_5 - ^3H_4$	[57]
Pr^{3+}	$Ga_2Ge_{30}As_6S_{62}$	1.1	4.7	$^3F_2, ^3H_6 - ^3H_5 + ^3H_5 - ^3H_4$	[58]
Pr^{3+}	$Ga_5Ge_{28}As_{12}S_{55}$	1.1	4.7	$^3F_2, ^3H_6 - ^3H_5 + ^3H_5 - ^3H_4$	[58]
Pr^{3+}	$GaGeAsSe$	2.0	4.8	$^3H_5 - ^3H_4$	[7]
Pr^{3+}	$GaGeAsSe$	2.0	4.0	$^3F_2, ^3H_6 - ^3H_5$	[7]
Pr^{3+}	$Ga_5Ge_{20}Sb_{10}Se_{65}$	2.0	4.8	$^3F_2, ^3H_6 - ^3H_5 + ^3H_5 - ^3H_4$	[59]
Pr^{3+}	$Ga_{0.5}Ge_{16.5}As_{18.5}S_{64.5}$	1.55	4.8	$^3F_2, ^3H_6 - ^3H_5 + ^3H_5 - ^3H_4$	[59]
Pr^{3+}	$GaGeAsSe$	1.55	4.8	$^3F_2, ^3H_6 - ^3H_5 + ^3H_5 - ^3H_4$	[60]
Pr^{3+}	$GaGeAsSe$	1.55/1.94	4.8	$^3F_2, ^3H_6 - ^3H_5 + ^3H_5 - ^3H_4$	[61]
Pr^{3+}	$Ga_2Ge_{30}Sb_8Se_{60}$	1.48/2.05	4.8	$^3F_2, ^3H_6 - ^3H_5 + ^3H_5 - ^3H_4$	[62]
Ho^{3+}	$GeS_2 - GeS_2 - Sb_2S_3$	0.756	4.00	$^5I_5 - ^5I_6$	[63]
Ho^{3+}	$GeS_2 - GeS_2 - Sb_2S_3$	0.756	4.80	$^5I_4 - ^5I_5$	[63]
Ho^{3+}	$70GeS_2S_3 : 30La_2S_3$	0.756	3.90	$^5I_5 - ^5I_6$	[64]
Ho^{3+}	$70GeS_2S_3 : 30La_2S_3$	0.756	4.90	$^5I_4 - ^5I_6$	[64]
Dy^{3+}	$Ga{:}La{:}S$	0.815	4.27	$^6H_{11/2} - ^6H_{13/2}$	[65]
Dy^{3+}	$Ga_5Ge_{25}Sb_{10}Se_{60}$	1.3	4.35	$^6H_{11/2} - ^6H_{13/2}$	[67]
Dy^{3+}	$GaGeAsSe$	1.3	4.5	$^6H_{11/2} - ^6H_{13/2}$	[7]
Dy^{3+}	$Ga_5Ge_{25}S_{70}$	0.808	4.38	$^6H_{11/2} - ^6H_{13/2}$	[66]
Dy^{3+}	$Ga_5Ge_{30}Sb_5Se_{60}$	1.8	4.4	$^6H_{11/2} - ^6H_{13/2}$	[67]
Dy^{3+}	$Ga_5Ge_{25}Sb_{10}Se_{60}$	1.3	4.35	$^6H_{11/2} - ^6H_{13/2}$	[57]
Tb^{3+}	$GaGeAsSe$	1.97	4.80	$^7F_5 - ^7F_6$	[7]
Tb^{3+}	$GaGeAsSe$	1.97	7.50	$^7F_4 - ^7F_5$	[7]
Tb^{3+}	$GaGeAsSeI$	2.94	4.8	$^7F_5 - ^7F_6$	[68]

(continued)

Table 2.2 (continued)

Dopants	Host glass	Pump $\lambda(\mu m)$	Emission $\lambda(\mu m)$	Transition	Reference
Tb^{3+}	$70GeS_2S_3 : 30La_2S_3$	0.8	4.8	${}^7F_5 - {}^7F_6$	[69]
Tb^{3+}	$GaGeAsTe$	NA	4.80	${}^7F_5 - {}^7F_6$	[70]
Tb^{3+}	$GaGeAsSTe$	NA	7.50	${}^7F_4 - {}^7F_5$	[70]
Er^{3+}	$Ga_5Ge_{25}Sb_{10}Se_{60}$	0.810	4.53	${}^4I_{9/2} - {}^4I_{11/2}$	[71]
Er^{3+}	$70GeS_2S_3 : 30La_2S_3$	0.810	4.53	${}^4I_{9/2} - {}^4I_{11/2}$	[72]
Tm^{3+}	$70GeS_2S_3 : 30La_2S_3$	0.8	3.88	${}^5H_5 - {}^3F_4$	[73]

doped with 0.05% Nd_2S_3 with an outer diameter of 230 μm. The laser had a 0.7% slope efficiency [56]. Several factors have to be taken into account to construct an efficient mid-infrared laser based on a chalcogenide glass host. First, as mentioned before, is the manufacture of high purity glass with a low optical loss level at pump and emission wavelengths. Secondly, both the upper and lower laser manifolds possess long lifetimes in comparison to the ground state. This causes self-terminating laser operation and makes achieving population inversion difficult [5–7, 53–73]. In Sect. 2.6 the authors' solution to overcome this problem will be presented. Another problem that occurs in doped chalcogenide glass is crystallisation; it can influence the loss via scattering [53–55].

Recently, many research groups have reported experimental emission from rare earth doped chalcogenide glasses. However only limited numbers of papers report on emission at wavelengths beyond 3.5 μm. Figure 2.7 provides a simplified Dieke diagram, containing only the mid-infrared transitions reported in the rare earth doped chalcogenide glasses. A selected summary of emission at wavelengths beyond 3.5 μm reported in rare earth doped chalcogenide glasses is shown in Table 2.2. Table 2.2 includes rare earth dopant, host glass composition, pump wavelength, emission wavelength, transition and quantum efficiency.

The limited number of research groups which has been able to achieve mid-infrared emission from chalcogenide glass indicates that the technology of fabrication and characterisation of these glasses is challenging.

2.4 Obtaining Spectroscopic Parameters as Inputs to the Numerical Model

In this section we describe the experimental procedures that are used to obtain the spectroscopic parameters for modelling lanthanide doped fibre lasers. The most important parameters that are needed for modelling lasers are absorption cross-section, emission cross-section and the photoluminescence lifetimes. These parameters are determined indirectly from measurements.

2.4.1 Absorption Cross-Section Measurements

The definition of absorption cross-section has already been given in Sect. 2.2.2. Absorption cross-section is experimentally extracted for a bulk sample by comparing the transmission spectra without and with the presence of the bulk glass sample. Absorption of light in a medium is described by Lambert–Beer law as follows [16–19]:

$$I(L) = I_0(0) \times e^{-\alpha L} \tag{2.19}$$

where I(L) is the light intensity with the glass sample present, I_0 is the light intensity without the glass sample, α is the absorption coefficient, and L is the sample thickness. The absorption cross-section can be calculated in the bulk sample from the concentration doping (N) and absorption coefficient using following equation:

$$\sigma_a(\nu) = \frac{\alpha}{N} \tag{2.20}$$

where $\sigma_a(\nu)$ is absorption cross-section, N is the number density, for example ions/m^3. Experimentally, the absorption cross-section can be directly measured using a broadband light source (for example tungsten lamp or Globar heat sources) and a spectrometer (for example FTIR (Fourier Transform Infrared Spectroscopy) or grating monochromator) [16–19].

2.4.2 Emission Cross-Section Measurements

The emission cross-section can be obtained from photoluminescence spectral shape measurements and scaled using the Fuchtbauer–Ladenburg (F-L) equation, given by [16–19]:

$$\sigma_e = \frac{\lambda^4}{8\pi n^2 c} \times A_{jj'} \Delta\lambda \tag{2.21}$$

where $\Delta\lambda = I(\lambda)/\int I(\lambda) d\lambda$ is the line-shape of the emission band, $I(\lambda)$ is the blackbody-calibrated emission intensity, n is the refractive index, c is the speed of light in a vacuum, Ajj' is the spontaneous emission rate of the transition and λ is the central wavelength of the emission [16–19].

It is important to emphasise that in order to accurately calculate the emission cross-section the photoluminescence spectral shape should be calibrated by the blackbody response of the system. Additionally the photoluminescence spectral shape should be free from re-absorption and contributions from other unwanted transitions. The basic experimental setup used in fluorescence measurements is shown in Fig. 2.8. The fluorescence set-up consists of a laser pump, chopper, lock- in amplifier, optical detector conjugate with preamplifier and also a data acquisition card and a computer. Normally the fluorescence signal is very low, therefore in order to increase the signal-to-noise ratio of the fluorescence signal it is modulated by the chopper, and only signals with this particular modulation frequency are recorded by the lock-in amplifier.

2.4.3 Lifetime Measurements

The definition of lifetime of rare earth doped materials has been already given in Sect. 2.2.3. In this subsection the experimental procedure of extracting the lifetime

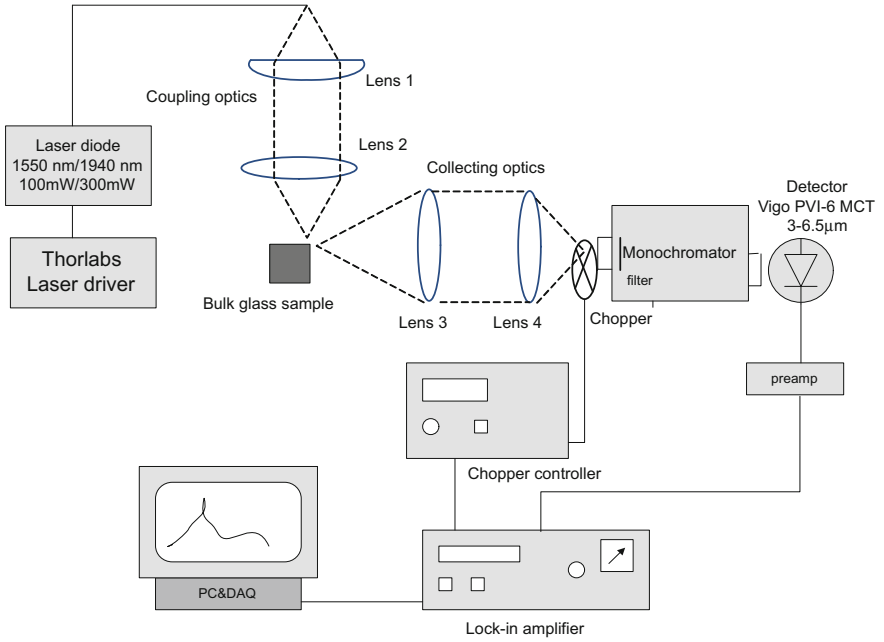

Fig. 2.8 Experimental setup for mid-infrared emission measurements

is briefly described. The decay lifetimes of emission are measured by exciting the ions from the ground state to upper states using a pulsed laser diode. Most of the ions should return spontaneously to the ground state or lower energy levels. From a practical point of view the period when pump is off should be at least five times longer than the measured lifetime in order to provide sufficient time for proper sampling of the fluorescence signal. Additionally, the time response of the system should be at least 1/10 of the lifetime which is to be measured. The value of the lifetime can be found by fitting experimental data to a single exponential function using a least squares algorithm. The fitting function is described by [16–19]:

$$I(t) = I_0 \times exp\left(-\frac{t}{\tau}\right) \tag{2.22}$$

where, I_0 is the intensity before the pump is switched off and τ is the fluorescence lifetime [16–19]. The experimental set-up for measuring the photoluminescence lifetime is presented in Fig. 2.9. It consists of a pulsed pump laser, a monochromator (set to the particular wavelength for which the lifetime will be measured), optical detector connected with preamplifier and also an oscilloscope and a computer. In order to increase signal-to-noise ratio the fluorescence decay signals should be collected many times and results averaged. In our case the fluorescence decay signal was measured 10000 times and subsequently averaged.

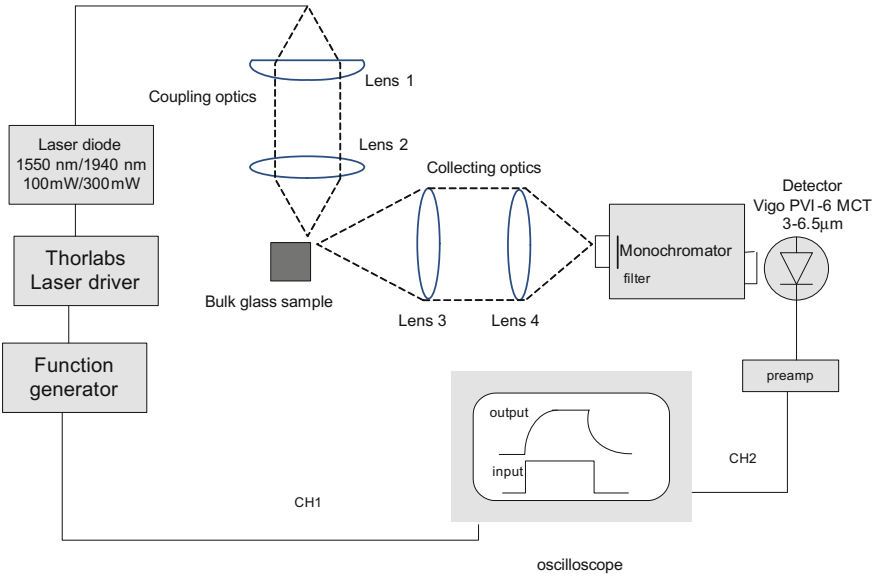

Fig. 2.9 Experimental setup for photoluminescence decay measurements

2.5 Models for Fibre Lasers

Numerical modelling can be used to evaluate fibre laser parameters. Parameters like optimum fibre length, output power, and optimum pump wavelength and pump power, fibre waveguide geometry and laser slope efficiency can also be predicted using a numerical fibre laser model. All this information is crucial for designing experimental fibre lasers [75–97]. The basic properties of a fibre laser can be analysed using the rate population equation, as introduced initially in Sect. 2.2.6, and a propagation equation for the pump and signal beams. The spectroscopic parameters of the lanthanide doped material are needed as inputs for the numerical model. Basic parameters required for the modelling are the absorption and emission cross-sections at pump and signal wavelengths, the photoluminescence lifetimes and the photoluminescence branching ratios. These parameters have been introduced in Sect. 2.2 [16–20]. The spectroscopic parameters can be extracted from spectroscopic measurements using the methods described in Sect. 2.4. The modelling results presented in this section are based on the measured spectroscopic parameters.

In order to explain the laser modelling a Pr^{3+} doped chalcogenide fibre laser will be considered as a illustrating example. The Pr^{3+} laser system has been chosen because the explanation of this laser scheme should help the Reader understand the further experimental and modelling results that will be presented in this chapter.

Praseodymium has strong absorption bands at wavelengths around 1.55 and 2 μm. For our purpose the band at 2 μm will be used. This band can be easily covered by available semiconductor diodes in an (AlGaIn) (AsSb) material system technology, and also with solid state lasers doped with thulium and holmium [80–85]. The power level generated by these sources is in the range of hundreds of Watts. In this chapter we will propose the idea of a cascade laser pumped by 2 μm sources and based on praseodymium doped chalcogenide glass fibre. The principal problem with pumping praseodymium doped chalcogenide glass with a light source at 2 μm is that the level $(^3F_2, ^3H_6) \longrightarrow ^3H_5$ has a long lifetime, circa 2.7 ms [7]. This causes the carrier population to accumulate in this level, which results a substantial depletion of the ground state. This reduces the power that can be absorbed per unit length of fibre and consequently the output power. In order to de-excite the $(^3F_2, ^3H_6) \longrightarrow ^3H_5$ transition a cascade laser structure is proposed [86–88]. In a cascade laser structure two transitions, are simultaneously stimulated in the active fibre. Through simultaneous lasing of the two wavelengths corresponding to these transitions, the upper level is sufficiently depopulated so that efficient laser operation is achieved. Cascade operation of the two laser transitions $(^3F_2, ^3H_6) \longrightarrow ^3H_5$ and $^3H_5 \longrightarrow ^3H_4$, so that they occur simultaneously, can be an alternative solution to deplete the $(^3F_2, ^3H_6) \longrightarrow ^3H_5$ populations [85–90]. We have proposed such a scheme for a Pr^{3+} chalcogenide glass fibre laser.

The 3 level lasing system is presented in Fig. 2.10. The laser design shown in Fig. 2.11 relies on the feedback provided by Bragg gratings inscribed into chalcogenide glass. Another advantage of the cascade configuration is that the level $(^3F_2, ^3H_6) \longrightarrow ^3H_5$ transitions are depopulated in a radiative way so that they do not generate additional heat compared with a nonradiative process. This feature is desirable in chalcogenide glass materials where the glass softening temperatures are much lower than in silica glass [6].

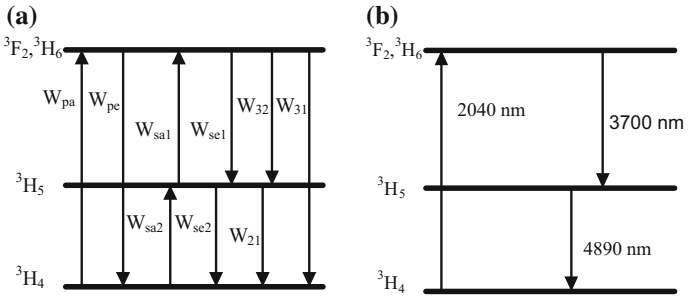

Fig. 2.10 **a** Schematic energy level scheme of Pr^{3+}GeAsGaSe fibre, showing probabilities of absorption (a), emission (e) and spontaneous emission (ij).The transition rates depicted in Fig. 2.10a are defined as follows: the absorption and emission rates W_{pa},W_{pe},W_{sa1},W_{se1}, W_{sa2},W_{se2} of pump and signals respectively, W_3=W_{31}+W_{32} the spontaneous decay rate of level 3, W_{21} the spontaneous decay rate of level 2. **b** Simplified energy level diagram of Pr^{3+} doped GeAsGaSe fibre, showing cascade laser transitions

Fig. 2.11 Cascade laser scheme in Pr^{3+} doped chalcogenide fibre with fibre Bragg gratings

2.5.1 Laser Rate and Propagation Equations

In order to calculate the laser performance one needs to know the spatial distribution of the volume concentration of atoms in the various energy levels. The atom concentrations are usually calculated using a rate equations approach. For the energy levels shown in Fig. 2.10a the rate equations for the population densities N_i in the Pr^{3+} chalcogenide glass system are given by [78, 86–88]:

$$\frac{dN_3}{dt} = W_{pa}N_1 + W_{sa1}N_2 - (W_{pe} + W_{se1} + W_{31} + W_{32})N_3 \tag{2.23}$$

$$\frac{dN_2}{dt} = W_{sa2}N_1 - (W_{se2} + W_{21} + W_{sa1})N_2 + (W_{se1} + W_{32})N_3 \tag{2.24}$$

$$\frac{dN_1}{dt} = -(W_{pa} + W_{sa2})N_1 + (W_{se2} + W_{21})N_2 + (W_{pe} + W_{31})N_3 \tag{2.25}$$

The rate equations describe the rate of change of the population densities N_1, N_2 and N_3 as a result of absorption and stimulated emission, as well as radiative and nonradiative transitions. These phenomena were described in detail in Sect. 2.2. For example the net rate of change of the atom concentration in level 3 is increased by the pump rate W_{pa} and the stimulated absorption rate W_{sa1} and decreased by the stimulated emission rate W_{se1}, pump emission rate W_{pe} and spontaneous emission rates W_{32} and W_{31}.

In the steady state ($\frac{dN_i}{dt} = 0$) the (2.23)–(2.25) reduce to three algebraic equations. The (2.23)–(2.25) are not linearly independent so each equation is determined by all others. However they can be connected through the simple relation of particle conservation [16–19]:

$$N = N_1 + N_2 + N_3 \tag{2.26}$$

The (2.26) follows from the principle that the sum of atom densities in all energy levels should be equal to the total Pr^{3+} concentration in the host glass.

In order to find a solution of the rate equation in the steady state ($\frac{dN_i}{dt} = 0$), these equations can be re-written using matrix notation:

$$\begin{bmatrix} -(W_{pa}+W_{sa2}) & (W_{se2}+W_{21}) & (W_{pe}+W_{31}) \\ W_{sa2} & -(W_{se2}+W_{21}+W_{sa1}) & (W_{se1}+W_{32}) \\ 1 & 1 & 1 \end{bmatrix} \begin{bmatrix} N_1 \\ N_2 \\ N_3 \end{bmatrix} = \begin{bmatrix} 0 \\ 0 \\ N \end{bmatrix} \quad (2.27)$$

Using simple algebra N_1, N_2 and N_3 can easily be obtained. In (2.23)–(2.27) the stimulated emission or absorption rates are expressed by

$$W_{xy} = \frac{\Gamma_x \sigma_{xy} \lambda_x (P_x^+ + P_x^-)}{Ahc} \quad (2.28)$$

where Γ_x is the overlap factor, which defines the fraction of energy that propagates in the core to the total energy that propagates in the fibre (core and clad), σ_{xy} is the absorption or emission cross-section for the xy transition (see Sects. 2.2.2 and 2.4), P_x^+ and P_x^- denote the forward and backwards propagating signal, and pump powers respectively, A-is the doping cross-section area, h is Planck's constant, λ_x is the wavelength of signals or pump and c is the speed of light in free space.

The spontaneous emission probability per unit time between levels i and j is denoted by W_{ij}. The radiative lifetime of Level 3 is then $\tau_3 = 1/(W_{31} + W_{32})$ and the branching ratio for the $3 \longrightarrow 2$ transition is $\beta_{32} = W_{32}/(W_{31} + W_{32})$. The branching ratio has been described in Sect. 2.2.5. The optical power that propagates through the doped fibre core or cladding region can be related with photon flux using [16–20]:

$$P_x = \frac{\phi_x h \nu_x A}{\Gamma_x} \quad (2.29)$$

The photon flux and intensity definitions are given in Sect. 2.2.1. The propagation of pump and signal powers P_p, P_{s1}, P_{s2} respectively along the active fibre is described by the following differential equations [16–20]:

$$\frac{dP_p^{\pm}}{dz} = \pm \Gamma_p (\sigma_{pe} N_3 - \sigma_{pa} N_1) P_p^{\pm} \mp \alpha_p P_p^{\pm} \quad (2.30)$$

$$\frac{dP_{s1}^{\pm}}{dz} = \pm \Gamma_{s1} (\sigma_{32e} N_3 - \sigma_{32a} N_2) P_{s1}^{\pm} \mp \alpha_{s1} P_{s1}^{\pm} \quad (2.31)$$

$$\frac{dP_{s2}^{\pm}}{dz} = \pm \Gamma_{s2} (\sigma_{21e} N_2 - \sigma_{21a} N_1) P_{s2}^{\pm} \mp \alpha_{s2} P_{s2}^{\pm} \quad (2.32)$$

where + and − refer to forward and backward travelling waves, respectively, $P_p^{\pm} = P_p^+ + P_p^-; P_{s1}^{\pm} = P_{s1}^+ + P_{s1}^-; P_{s2}^{\pm} = P_{s2}^+ + P_{s2}^-$.

In order to solve the propagation equations numerically they need to be expressed in a discrete form. According to the first order derivative the propagation equations can be discretised into the form:

$$\frac{P_p^+(i+1)-P_p^+(i)}{dz} = \Gamma_p(\sigma_{pe}N_3 - \sigma_{pa}N_1)P_p^+(i) - \alpha_p P_p^+(i) \tag{2.33}$$

$$\frac{P_p^-(i-1)-P_p^-(i)}{dz} = -\Gamma_p(\sigma_{pe}N_3 - \sigma_{pa}N_1)P_p^-(i) + \alpha_p P_p^-(i) \tag{2.34}$$

$$\frac{P_{s1}^+(i+1)-P_{s1}^+(i)}{dz} = \Gamma_{s1}(\sigma_{32e}N_3 - \sigma_{32a}N_2)P_{s1}^+(i) - \alpha_{s1} P_{s1}^+(i) \tag{2.35}$$

$$\frac{P_{s1}^-(i-1)-P_{s1}^-(i)}{dz} = -\Gamma_{s1}(\sigma_{32e}N_3 - \sigma_{32a}N_2)P_{s1}^-(i) + \alpha_{s1} P_{s1}^-(i) \tag{2.36}$$

$$\frac{P_{s2}^+(i+1)-P_{s2}^+(i)}{dz} = \Gamma_{s2}(\sigma_{21e}N_2 - \sigma_{21a}N_1)P_{s2}^+(i) - \alpha_{s2} P_{s2}^+(i) \tag{2.37}$$

$$\frac{P_{s2}^-(i-1)-P_{s2}^-(i)}{dz} = -\Gamma_{s2}(\sigma_{21e}N_2 - \sigma_{21a}N_1)P_{s2}^-(i) + \alpha_{s2} P_{s2}^-(i) \tag{2.38}$$

The propagation equations (2.30)–(2.38) describe the rate of change of pump and signal photon flux as a function of the fibre length. The incremental number of photons gained is the difference between the stimulated emission rate and the stimulated absorption rate. Generally the propagation equation represents the net gain in the photon flux density per unit length (see also Sect. 2.2.6). The (2.34)–(2.38) are presented in the form of the first-order Runge–Kutta equations. In such a form they can be easy implemented.

2.5.2 Boundary Conditions

At the fibre ends boundary conditions for pump and signal fluxes need to be included. These boundary conditions equate the forward and backward fields at either end of the fibre, taking into consideration the output coupling fraction and the incident pump light [75–97].

$$P_p^+(0) = R_{1p}P_p^-(0) + P_{pin} \tag{2.39}$$

$$P_p^-(L) = R_{2p}P_p^+(L) \tag{2.40}$$

$$P_{s1}^+(0) = R_{1\lambda 1}P_{s1}^-(0) \tag{2.41}$$

$$P_{s1}^-(L) = R_{2\lambda 1}P_{s1}^+(L) \tag{2.42}$$

$$P_{s2}^+(0) = R_{1\lambda 2}P_{s2}^-(0) \tag{2.43}$$

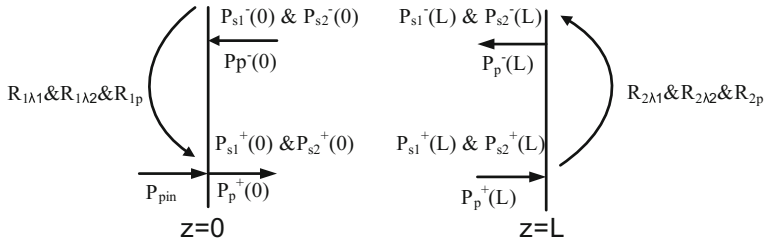

Fig. 2.12 Schematic illustration of boundary conditions depicting the position of the input and output mirrors at z = 0 and z = L, respectively. The input and output mirrors have reflectivities of ($R_{1\lambda1}$,$R_{1\lambda2}$,R_{1p}) and ($R_{2\lambda1}$, $R_{2\lambda2}$, R_{2p}) respectively. The arrows show the direction of the forward (superscript '+') and backward (superscript '−') pump and signals [78, 82, 83]

$$P_{s2}^{-}(L) = R_{2\lambda2} P_{s2}^{+}(L) \tag{2.44}$$

Here it is assumed that the length of the fibre is L and stated that:
P_{pin} is the input pump power
$R_{1\lambda1}$ is the reflectivity of the input mirror at z=0 for signal wavelength λ_{s1}
$R_{1\lambda2}$ is the reflectivity of the input mirror at z=0 for signal wavelength λ_{s2}
R_{1p} is the reflectivity of the input mirror at z=0 for pump wavelength λ_p
$R_{2\lambda1}$ is the reflectivity of the output mirror at z=L for signal wavelength λ_{s1}
$R_{2\lambda2}$ is the reflectivity of the output mirror at z=L for signal wavelength λ_{s2}
R_{2p} is the reflectivity of the output mirror at z=L for pump wavelength λ_p
The boundary conditions for signals and pump have been imposed according to Fig. 2.12.

In order to calculate optical power with respect to input pump power the (2.23)–(2.45) have to be solved in a self-consistent manner with respect to the boundary conditions at the ends of the fibre. In mathematical terms, we need to solve a two-point boundary value problem. In order to resolve this problem sophisticated methods for the numerical integration of the ordinary differential equations must be applied. Therefore, convergence needs to be satisfied simultaneously in a multi-dimensional space. Well-known methods for solving such a two-point boundary value problem are the shooting method, the coupled solution method and a fixed point iteration method [86–94].

In the present work a fixed point iteration method was used, as will be described in Sect. 2.5.3. The physical simulation parameters used in the modelling of the fibre lasers are summarised in Table 2.3.

2.5.3 Numerical Calculation Procedure

The calculation procedure relies on solving the (2.24)–(2.45). To solve this set of equations the fibre of length L is divided into K segments along the longitudinal axis

Table 2.3 Fibre laser physical modelling parameters

Symbol	Quantity	Unit
r_{core}	Fibre core radius	μm
r_{clad}	Fibre clad radius	μm
A_{core}	Fibre core area	μm^2
A_{clad}	Fibre clad area	μm^2
L	Fibre length	m
N	Ion concentration	ions/cm^3
λ_{s1}	Signal 1 wavelength	μm
λ_{s2}	Signal 2 wavelength	μm
λ_p	Pump wavelength	μm
σ_{32a}	Signal 1 absorption cross-section	cm^2
σ_{32e}	Signal 1 emission cross-section	cm^2
σ_{21a}	Signal 2 absorption cross-section	cm^2
σ_{21e}	Signal 2 emission cross-section	cm^2
σ_{pa}	Pump absorption cross-section	cm^2
σ_{pe}	Pump emission cross-section	cm^2
Γ_{s1}	Overlap factor for singal 1	
Γ_{s2}	Overlap factor for singal 2	
Γ_p	Overlap factor for pump	
τ_3	Lifetime of level 3	ms
τ_2	Lifetime of level 2	ms
β_{32}	Branching ratio for 3-2 transition	
α_{s1}	Fibre loss at singal 1 wavelength	dB/m
α_{s2}	Fibre loss at singal 2 wavelength	dB/m
α_p	Fibre loss at pump wavelength	dB/m
P_p	Pump power	W

(see Fig. 2.13), which then yields a spatial resolution of dz=L/K. Each individual fibre segment contains its unique population densities, and pump and signals photon fluxes are calculated at the ends of the segment. Initially, all populations are considered to be in the ground-state ($N_1 = N$, $N_2 = N_3 = 0$). Photons fluxes are set to initial values. Calculated population densities and photons fluxes are initial values for the second segment of fibre. Based on these initial values the population densities and photons fluxes are calculated. The forward and backward propagating photon fluxes along the fibre are integrated using a Runge–Kutta (RK) routine. For example a RK algorithm can be implemented in Matlab using the standard ode 45 function which relies on a Dormand and Price version of the RK algorithm [78, 92]. In this manner the calculations are carried out until the end of the fibre is reached. At the end of the fibre a part of each of the photon fluxes is reflected by the mirror. In order to include this behaviour in the algorithm boundary conditions are imposed and the

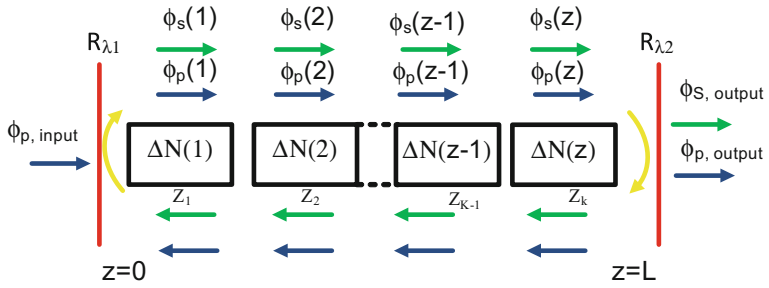

Fig. 2.13 Schematic of longitudinal discretisation in fibre laser cavity [78]

population equations are recalculated based on the new values of the photon fluxes. After reflection the beams are propagated in the counter direction in the same manner as before. This procedure is repeated until the photon flux values converge to within required tolerances. In the iteration procedure the convergence of the photon flux is checked and the iterative process is terminated once sufficient accuracy is achieved [78]. The convergence was checked using the following condition:

$$\frac{P_{s,out}^{j+1} - P_{s,out}^{j}}{P_{s,out}^{j}} = TOL \tag{2.45}$$

where TOL is the required tolerance, $P_{s,out}^{j+1}$ is the output power value from the last iteration, $P_{s,out}^{j}$ is the output power value from the previous iteration.

It was found by numerical experiment that the tolerance should be set smaller than 10^{-6}. The output signals powers were calculated as the fraction (1-$R_{2\lambda 1}$ and 1-$R_{2\lambda 2}$) of the forward signal powers.

2.5.4 Numerical Algorithm

The algorithm for modelling fibre lasers is presented below and summarised in the following steps [78]:

1. Setup initial values (pump and signals wavelengths, the longitudinal step of calculations $\Delta z = L/K$, confinement factors for pump and signal wavelengths)
2. Include initial values of pump and signals powers at z = 0
3. For i = 0 to K − 1

Calculate $N_1(z) = f(P_p^+, P_{s1}^+, P_{s2}^+, P_p^-, P_{s1}^-, P_{s2}^-)$, $N_2(z) = f(P_p^+, P_{s1}^+, P_{s2}^+, P_p^-, P_{s1}^-, P_{s2}^-)$, $N_3(z) = f(P_p^+, P_{s1}^+, P_{s2}^+, P_p^-, P_{s1}^-, P_{s2}^-)$ using (2.23)–(2.29)

Calculate $P_p^{\pm}$, $P_{s1}^{\pm}$, $P_{s2}^{\pm}$ using (2.30)–(2.38)

4. If z = L apply boundary conditions defined by (2.39–2.44)
5. For i = K to 1

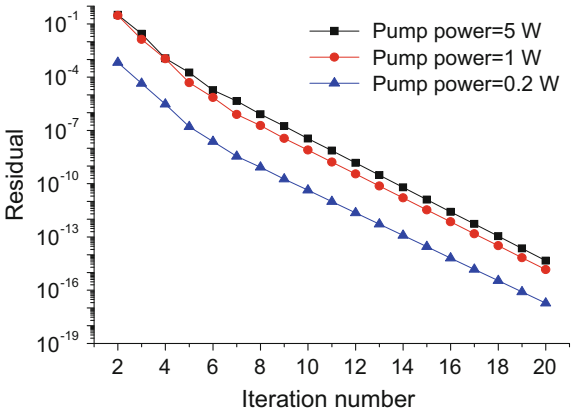

Fig. 2.14 Numerically calculated dependence of the residual for different input pump powers

Calculate $N_1(z) = f(P_p^+, P_{s1}^+, P_{s2}^+, P_p^-, P_{s1}^-, P_{s2}^-)$, $N_2(z) = f(P_p^+, P_{s1}^+, P_{s2}^+, P_p^-, P_{s1}^-, P_{s2}^-)$, $N_3(z) = f(P_p^+, P_{s1}^+, P_{s2}^+, P_p^-, P_{s1}^-, P_{s2}^-)$ using (2.23)–(2.29)
Calculate $P_p^{\pm}$, $P_{s1}^{\pm}$, $P_{s2}^{\pm}$ using (2.30)–(2.38)
6. If $z = 0$ apply boundary conditions defined by (2.39)–(2.44)
Check convergence (2.45)
If (P_{out}^{j+1})-(P_{out}^{j})>TOL go to step 3 and repeat until required convergence is achieved.

In order to prove that described numerical algorithm is robust the residual in function of iteration number for different pump powers has been calculated (see Fig. 2.14). It can be observed that slightly slower convergence takes place for higher input pump powers. However the developed algorithm converges rapidly and a self-consistent solution can be found after only a few iterations [78].

In this section, the numerical modelling of fibre lasers has been described. Specifically, the modelling of a Pr^{3+} doped chalcogenide fibre laser was studied as an illustrating example. The aim of this section was to introduce to the reader to the numerical procedures used in fibre laser modelling.

2.6 Numerical and Theoretical Studies of Mid-Infrared Laser Action in Chalcogenide Glasses Doped with Dy^{3+}, Pr^{3+} or Tb^{3+}

In this section an investigation of chalcogenide glass fibre lasers doped with dysprosium, praseodymium or terbium ions, that are proposed to work in the mid-infrared wavelength range, is reported. A series of chalcogenide glass samples doped with different concentrations of rare earth ions was manufactured. Modelling parameters were derived from FTIR absorption measurements on the manufactured bulk glass samples using Judd–Ofelt, Fuchtbauer—Ladenburg theory and McCumber theory [16–20]. The modelling results indicate that, for all the dopants considered, efficient laser action is achievable if optical losses are reduced to 1 dB/m or lower.

Table 2.4 Calculated spectroscopic parameters (fluorescence branching ratio and radiative lifetime) of Dy^{3+},Pr^{3+},Tb^{3+} in $Ge_{16.5}As_{16}Ga_3Se_{64.5}$ glass

Quantity	Dy^{3+}	Pr^{3+}	Tb^{3+}
Concentration	1000–2000 ppm	500–1500 ppm	500–1500 ppm
Lifetimes of level 3	2.2 ms	2.7 ms	5.9 ms
Lifetimes of level 2	6.1 ms	10.3 ms	11.8 ms
Branching ratio for 3–2 transition	0.0816	0.39	0.0876
Pump wavelength	1.71 μm	2.04 μm	2.95 μm
Signal wavelength (λ_1)	4.6 μm	4.89 μm	4.7 μm
Idler wavelength (λ_2)	3.20 μm	3.70 μm	None

2.6.1 Parameters Used in Modelling

Table 2.4 shows radiative lifetimes and branching ratios calculated from Judd–Ofelt method for the relevant transitions based on measured absorption spectra of Dy^{3+}, Pr^{3+}, Tb^{3+}. Other parameters presented in this Table, for example pump, signal and idler wavelength have been discussed in detail in Sect. 2.5.

From the FTIR measurements the absorption cross-sections were extracted in a straightforward manner. The emission cross-sections were derived from the absorption cross-section spectra using the McCumber theory (see Sect. 2.2.2) [16–20]. The shape of missing absorption and emission cross-sections (for 4 μm Pr^{3+}) was taken from [7] and scaled using lifetime and branching ratio values taken from Table 2.4. The spectral dependence of the emission and absorption cross-sections is presented in Fig. 2.15.

2.6.2 Modelling of Mid-Infrared Chalcogenide Fibre Lasers

Figure 2.16 depicts the energy level diagrams for the three lanthanide ion dopants studied (Dy^{3+}, Pr^{3+}, Tb^{3+}). In the case of Dy^{3+} and Pr^{3+}, obtaining mid-infrared laser action is not simple since both the upper and lower laser levels possess long decay lifetimes. Thus to mitigate this shortcoming a cascade laser configuration was applied. The cascade configuration involves adding a laser signal (or idler) that depopulates the lower or upper laser level. The cascade lasing configuration allows simultaneous operation of upper and lower laser levels, in this way both the levels are depopulated, mostly in a radiative way which reduces the heat generated. This configuration was proven experimentally in the case of Er:ZBLAN and Ho:ZBLAN fibre lasers [85, 89, 90]. The cascade fibre laser configuration is discussed in detail in Sect. 2.5 and also in [86–91]. In the case of Tb^{3+} doped chalcogenide glass the transitions from the $^7F_4$, $^7F_3$, $^7F_2$, $^7F_1$, $^7F_0$ levels are expected to be strongly quenched.

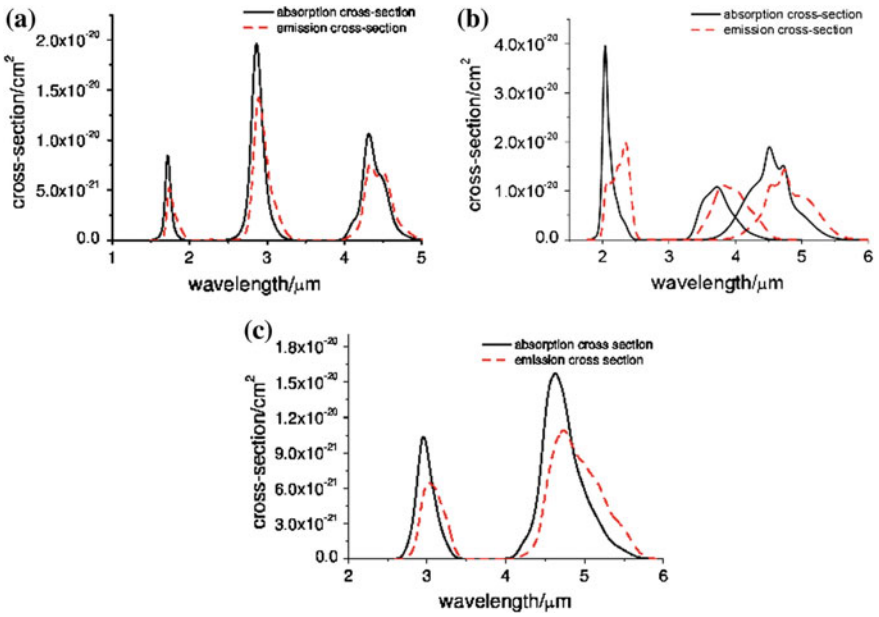

Fig. 2.15 Calculated emission and absorption cross-sections as a function of wavelength for **a** Dy^{3+}, **b** Pr^{3+} and **c** Tb^{3+} [86, 87]

Therefore the upper laser manifolds will relax quickly to the long-lived $^7F_5$ manifold. A mid-infrared 3-level laser action (4.7 μm) may thus be possible from the $^7F_5$ to the $^7F_6$ level. Thus Tb^{3+} does not need the cascade operation because an upper laser lever is depopulated in a nonradiative way. Therefore a laser model similar to that described in Sect. 2.5 was used; however it has been assumed that the upper transition was depopulated in a nonradiative way. Thus the idler was set to 0.

The numerical model used here, as described in Sect. 2.5, is based on a self-consistent solution of the level population rate equations and the optical propagation equations [86–91]. The fibre structure is assumed to be a double-clad one operating a single mode at both the signal and idler wavelengths, a core radius of 5.5 μm, and a clad with a radius of 30 μm which is multimode for the pump wavelength. The signal and idler wavelengths have been defined in Sect. 2.5. The possibilities of fabricating chalcogenide glass single mode fibre were proven in [49, 50]. The pump confinement factor was evaluated under the assumption of pump power being uniformly distributed throughout the fibre cladding. The confinement factors for the signal and the idler were evaluated using the mode field distribution calculated for the nominal wavelengths given in Table 2.4. A fibre laser resonator structure proposed in [86–88] is illustrated in Fig. 2.11 and contains two pairs of fibre Bragg gratings (FBG). The behaviour of a FBG in a laser cavity has been discussed in Sect. 2.2.8. One pair of gratings confines the signal, the other one the idler. The reflectivity of the input FBG for the pump wavelength is taken to be 0.05 while for the signal and

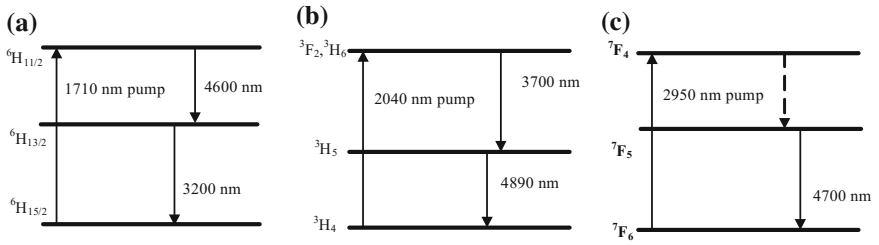

Fig. 2.16 Energy level diagram showing cascade laser transitions of **a** Dy^{3+}, **b** Pr^{3+} and **c** Tb^{3+} [86, 87]

the idler it is taken to be 0.95. The output reflectivity is taken as 0.05 for the signal and 0.9 for the idler. The fibre laser reflectivities were described in Sect. 2.2.8. The loss at all wavelengths is assumed to be 1 dB/m. (It can be noted that much lower loss levels have been realised experimentally for simple chalcogenide glass fibres [86–88]). In the case of Tb^{3+} doped selenide glass it has been assumed that only the signal laser wavelength is trapped in the laser cavity. Detailed information about the numerical modelling and modelling assumptions and parameters is given in Sect. 2.5. The remaining modelling parameters are presented in Table 2.4 and in Fig. 2.15.

2.6.3 Dy^{3+} Doped Chalcogenide Glass Fibre Laser

First, chalcogenide glass doped with Dy^{3+} was investigated. The energy level diagram is shown in Fig. 2.16a. The doping concentration assumed in the model is equal to 1500 ppmw (2.454×10^{19} ions/cm^3). For similar doping level manufactured chalcogenide bulk glass samples indicate no signs of crystallisation [54]. The laser action at 4.6 μm in Dy^{3+} doped glass can be achieved between the $^7H_{11/2}$ and $^7H_{13/2}$ levels by pumping the level $^7H_{11/2}$ with a 1.71 μm pump. The idler wavelength (levels $^7H_{13/2}$ and $^7H_{15/2}$) is set to 3.2 μm. Figure 2.17a shows the calculated signal power as a function of the fibre length and pump power. The slope efficiency at a wavelength of 4.6 μm reaches about 9%, which is in good agreement with the results quoted in [86–88].

2.6.4 Pr^{3+} Doped Chalcogenide Glass Fibre Laser

The next dopant investigated is praseodymium, Pr^{3+}. Pr^{3+} has substantial absorption bands at 1.55 and 2 μm. In this case pumping at around 2 μm is considered. The main issue with pumping Pr^{3+} doped chalcogenide glass at 2 μm is that the ($^3F_2$,$^3H_6$)states possess a relatively long lifetime, of about 2.7 ms. Therefore to

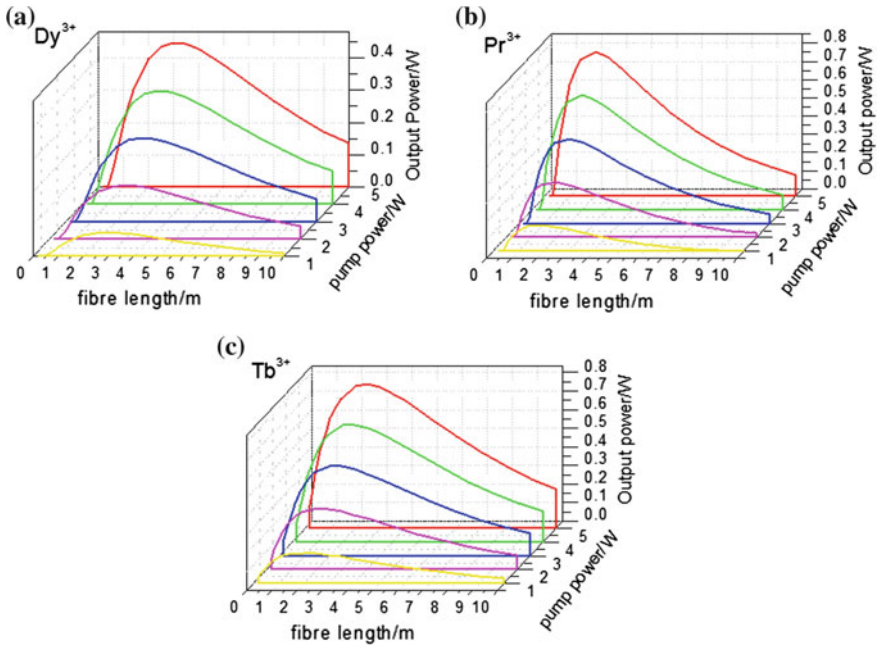

Fig. 2.17 Numerically calculated signal power as a function of fibre length with different pump power for **a** Dy^{3+}, where signal wavelength 4.6 μm, idler wavelength 3.2 μm, N = 1500 ppmw (2.4549×10^{19} ions/cm^3), α =1 dB/m, **b** Pr^{3+}, where signal wavelength 4.89 μm, idler wavelength 3.7 μm, N = 1500 ppmw (2.8395×10^{19} ions/cm^3), α = 1 dB/m, **c** Tb^{3+}, where signal wavelength 4.7 μm, idler wavelength set to 0), N = 1500 ppmw (2.51×10^{19} ions/cm^3), α = 1 dB/m [87]

de-excite the ($^3F_2$,$^3H_6$) level faster it is again proposed to use a cascade laser operation (see also Sect. 2.5). The FBG wavelengths for the signal and the idler are therefore fixed at 4.89 and 3.7 μm, respectively. Figure 2.17b depicts the calculated signal power as a function of the fibre length and pump power. The slope efficiency for 4.89 μm wavelength reaches about 16%. The better efficiency than for Dy^{3+} can be explained by Pr^{3+}'s larger absorption cross section at 2.04 μm. This enables the pump power to be absorbed much faster and be less impaired by the fibre losses [87].

2.6.5 *Fibre Lasers Based on Tb^{3+} Doping*

Here the laser action at 4.7 μm appears between the levels $^7F_5$ and $^7F_6$. The pumping wavelength is 2.95 μm and it can be obtained by commercially available Er:YAG lasers and also by Er^{3+} and Ho^{3+} doped ZBLAN fibre lasers [5, 12–15]. The fibre structure is the same as in the previous cases; in the resonator structure only the signal is trapped due to depopulation of upper laser transition in nonradiative way. Figure 2.17 presents the calculated power signal as a function of the fibre length and

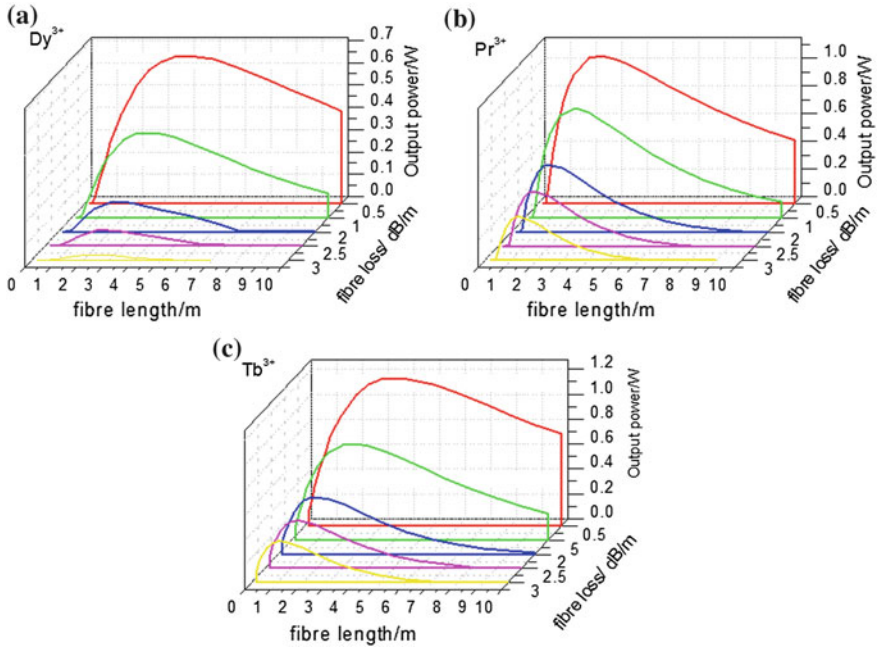

Fig. 2.18 Numerically calculated signal power as a function of fibre length with with different level of fibre optical losses **a** Dy^{3+}, **b** Pr^{3+} and **c** Tb^{3+}. The result were obtained with input pump power $P_p = 5$ W [87]

pump power. The results prove that efficient laser action at 4.7 μm is possible. The slope efficiency reaches about 15%. These results show that Tb^{3+} doped chalcogenide glass is a suitable choice for the future experimental development of the first fibre laser working at 4.7 μm wavelength.

Figure 2.18 presents the calculated output power as a function of the fiber length for selected values of the fibre loss. In all cases the doping concentration is 1500 ppmw and the pump power is 5 W. These results indicate that reasonable output power can be obtained even when losses are as high as 3 dB/m.

2.6.6 Summary

In this section the possibility of attaining a mid-infrared laser based on rare earth doped chalcogenide glass fibres was examined. Based on the experimentally extracted parameters and numerical modelling the possibility of lasing in chalcogenide glasses doped with Dy^{3+}, Pr^{3+} and Tb^{3+} was investigated. The results of our numerical modelling suggest that in all cases considered efficient laser action (with an efficiency of about 9–16%) can be obtained if the fibre losses are reduced to the 1 dB/m level.

2.7 Concluding Remarks

The background of laser physics has been reviewed in this chapter (Sect. 2.2). Fibre lasers were introduced and reviewed in Sect. 2.2.10. In Sect. 2.3 the recent progress in mid-infrared sources has been presented. The main aim of the work described in this chapter was to construct the first mid-infrared fibre laser. Thus the review has been devoted to rare earth doped chalcogenide rare earth doped glasses materials as a candidate for mid-infrared fibre lasers. Basic spectroscopic measurements used to extract modeling parameters have been described briefly in Sect. 2.4. In Sect. 2.5, the numerical modelling of fibre lasers has been presented. Specifically, the modelling of a Pr^{3+} doped chalcogenide fibre laser was studied as an illustrating example. Finally, (Sect. 2.6) the possibility of realising a mid-infrared laser based on Dy^{3+}, Pr^{3+} and Tb^{3+} doped chalcogenide glass fibres was investigated. In order to find the parameters for fibre laser models a set of chalcogenide samples doped with Dy^{3+}, Pr^{3+} and Tb^{3+} has been fabricated, and spectroscopically characterised. According to the experimental results, and numerical modelling, the feasibility of lasing in chalcogenide glasses doped with Dy^{3+}, Pr^{3+} and Tb^{3+} was investigated. Initial modelling was used to predict optimum fibre lengths, dopant concentrations and efficient pumping and lasing schemes. The numerical modelling results indicate that in all cases considered an efficient laser action (efficiency about 8–16%) is achievable in the cascade configuration provided the fibre losses are reduced to the 1 dB/m level.

Acknowledgements This research has been partly supported by the European Commission through the framework Seven (FP7) project MINERVA (317803; www.minerva-project.eu)

References

1. M. Ebrahim-Zadeh, I.T. Sorokina (eds.), *Mid-infrared coherent sources and applications, NATO Science for Peace and Security, Series B: Physics and Biophysics* (Springer, The Netherlands, 2008)
2. http://www.rp-photonics.com/highpowerfiberlasers.pdf
3. Y. Ma, R. Lewicki, M. Razeghi, F.K. Tittel, QEPAS based ppb-level detection of CO and N2O using a high power CW DFB-QCL. Opt. Express **21**, 1008 (2013)
4. B. Guo, Y. Wang, C. Peng, H. Zhang, G. Luo, Le, H., Gmachl, C., Sivco D., Peabody M., Cho A. Laser-based mid-infrared reflectance imaging of biological tissues. Opt. Express **12**, 208 (2004)
5. S. Jackson, Towards high-power mid-infrared emission from a fibre laser, Nat. Photon. **6**, 423 (2012)
6. A.B. Seddon, Z. Tang, D. Furniss, S. Sujecki, T.M. Benson, Progress in rare-earth-doped mid-infrared fiber lasers. Opt. Express **18**, 26704 (2010)
7. L.B. Shaw, B. Cole, P.A. Thielen, J.S. Sanghera, I.D. Aggrawal, Mid-wave IR and long-wave IR laser potential of rare-earth doped chalcogenide glass fiber. IEEE J. Quant. Electron. **37**, 1127 (2001)
8. J. Schneider, C. Carbonnier, U.B. Unrau, Characterization of a Ho^{3+}-doped fluoride fiber laser with a 3.9-μm emission wavelength. Appl. Opt. **36**, 8595 (1997)
9. H. Tobben, Room temperature cw fibre laser at 3.5 μm in Er^{3+}-doped ZBLAN glass. Electron. Lett. **28**, 1361 (1992)

10. C. Gautam, A.K. Yadav, A. K. Singh, A review on infrared spectroscopy of borate glasses with effects of different additives, ISRN Ceram. **2012**, 17 (2012)
11. J.S. Sanghera, L.B. Shaw, L.E. Busse, V.Q. Nguyen, P.C. Pureza, B.C. Cole, B.B. Harrison, I.D. Aggarwal, R. Mossadegh, F. Kung, D. Talley, D. Roselle, R. Miklos, Development and infrared applications of chalcogenide glass optical fibers, Fiber Integr. Opt. **19**, 251 (2000)
12. C. Carbonnier, H. Tbben, U.B. Unrau, Room temperature CW fibre laser at 3.22 μm. Electron. Lett. **34**, 893 (1998)
13. J.F. Li, D.D. Hudson, S.D. Jackson, High-power diode-pumped fiber laser operating at 3 μm. Opt. Lett. **36**, 3642 (2011)
14. O. Henderson-Sapir, J. Munch, D. Ottaway, Mid-infrared fiber lasers at and beyond 3.5 μm using dual-wavelength pumping. Opt. Lett. **39**, 493 (2014)
15. A. Berrou, C. Kieleck, M. Eichhorn, Mid-infrared lasing from Ho^{3+} in bulk InF3 glass. Opt. Lett. **40**, 1699 (2015)
16. R.S. Quimby, *Photonics and Lasers: An Introduction* (Wiley, New York, 2006)
17. B.E.A. Saleh, M.C. Teich, *Photons and Atoms, in Fundamentals of Photonics* (Wiley, New York, 2001)
18. P.C. Becker, N.A. Olsson, J.R. Simpson, Erbium-doped fiber amplifiers-amplifier basics, *Erbium-Doped Fiber Amplifiers* (Academic Press, San Diego, 1999), pp. 131–152
19. M.J.F. Digonnet, *Rare-Earth-Doped Fiber Lasers and Amplifiers*, 2nd edn. (Academic Press, CRC Press, Boca Raton, 2001)
20. Z. Burshtein, Radiative, nonradiative, and mixed-decay transitions of rare-earth ions in dielectric media Opt. Eng. **49**, 091005 (2010)
21. G.P. Agrawal, *Nonlinear Fiber Optics* (Academic Press, Cambridge, 2001)
22. G.P. Agrawal, *Fiber-Optic Communication Systems* (Wiley, New York, 2002)
23. E. Snitzer, Proposed fiber cavities for optical masers. J. Appl. Phys. **23**, 36 (1961)
24. C.J. Koester, E. Snitzer, Amplification in a fiber laser. Appl. Opt. **3**, 1182 (1964)
25. Y. Jeong, J. Sahu, D. Payne, J. Nilsson, Ytterbium-doped large-core fiber laser with 1.36 kW continuous-wave output power. Opt. Express **12**, 6088 (2004)
26. R.J. Mears, L. Reekie, M. Jauncey, D.N. Payne, Neodymium-doped silica single-mode fibre lasers. Electron. Lett. **26**, 1026 (1987)
27. E. Snitzer, Optical maser action of Nd^{3+} in a barium crown glass. Phys. Rev. Lett. **7**, 444 (1961)
28. J. Stone, C.A. Burrus, Neodymium-doped fiber fasers: room temperature cw operation with an injection laser pump. Appl. Opt. **13**, 41256 (1974)
29. W.L. Barnes, W.J. Barnes, S.B. Poole, J.E. Townsend, L. Reekie, D.J. Taylor, D.N. Payne, Er^{3+}-Yb^{3+} and Er^{3+} doped fiber lasers. J. Lightwave Technol. **7**, 1461 (1989)
30. B.C. Dickinson, P.S. Golding, M. Pollnau, T.A. King, S.D. Jackson, Investigation of a 791-nm pulsed-pumped 2.7-μm Er-doped ZBLAN fibre laser. Opt. Commun. **191**, 315 (2001)
31. D.J. Richardson, J. Nilsson, W.A. Clarkson, High power fiber lasers: current status and future perspectives [Invited]. J. Opt. Soc. Am. B **27**, B63 (2010)
32. V. Dominic, S. MacCormack, R. Waarts, S. Sanders, S. Bicknese, R. Dohle, E. Wolak, P.S. Yeh, E. Zucker, 110 W fibre laser. Electron. Lett. **35**, 1158 (1999)
33. A. Tnnermann, T. Schreiber, Limpert."Fiber lasers and amplifiers: an ultrafast performance evolution". J Appl. Opt. **49**, F71 (2010)
34. E. Snitzer, R. Woodcock, J. Segre, Phosphate glass Er^{3+} laser IEEE. J. Quantum Electron. **4**, 360 (1968)
35. R. Paschotta, J. Nilsson, A.C. Tropper, D.C. Hanna, Ytterbium-doped fiber amplifiers. IEEE J. Quantum Electron. **33**, 1049 (1997)
36. S. Xu, C. Li, W. Zhang, S. Mo, C. Yang, X. Wei, Z. Feng, Q. Qian, S. Shen, M. Peng, Q. Zhang, Z. Yang, Low noise single-frequency single-polarization ytterbium-doped phosphate fiber laser at 1083 nm. Opt. Lett. **38**, 501 (2013)
37. H. Scheife, G. Huber, E. Heumann, S. Bar, E. Osiac, Advances in up-conversion lasers based on Er^{3+} and Pr^{3+}. Opt. Mater. **26**, 365 (2004)
38. S.D. Jackson, M. Pollnau, Li,"Diode pumped erbium cascade fiber lasers". IEEE J. Quantum Electron. **47**, 471 (2011)

39. W.J. Miniscalco, Erbium-doped glasses for fiber amplifiers at 1500 nm. IEEE J. Lightwave Technol. **9**, 234 (1991)
40. L. Li, A. Schlzgen, V.L. Temyanko, T. Qiu, M.M. Morrell, Q. Wang, A. Mafi, J.V. Moloney, N. Peyghambarian, Short-length microstructured phosphate glass fiber lasers with large mode areas. Opt. Lett. **30**, 1141 (2005)
41. L. Yan, C.H. Lee, Thermal effects in end-pumped Nd: phosphate glasses. J. Appl. Phys. **75**, 1286 (1994)
42. S. Hollitt, N. Nikita, A. Hemming, J. Haub, A. Carter, A linearly polarised, pulsed Ho-doped fiber laser. Opt. Express **20**, 16285 (2012)
43. R. Paschotta, P.R. Barber, A.C. Tropper, D.C. Hanna, Characterization and modeling of thulium: ZBLAN blue upconversion fiber lasers. J. Opt. Soc. Am. B **14**, 1213 (1997)
44. P.F. Moulton, G.A. Rines, E.V. Slobodtchikov, K.F. Wall, G. Frith, B. Samson, A.L.G. Carter, Tm-Doped Fiber Lasers: Fundamentals and power scaling. IEEE J. Sel. Top. Quantum Electron. **15**, 1585 (2009)
45. J. Wu, Z. Yao, J. Zong, S. Jiang, Highly efficient high-power thulium-doped germanate glass fiber laser. Opt. Lett. **32**, 638 (2007)
46. H. Zellmer, K. Plamann, G. Huber, H. Scheife, A. Tunnermann, Visible double-clad upconversion fibre laser. Electron. Lett. **34**, 565 (1998)
47. R.G. Smart, D.C. Hanna, A.C. Tropper, S.T. Davey, S.F. Carter, D. Szebesta, A 20 dB gain thulium-doped fluorozirconate fibre amplifier operating at around 0.8 μm. Electron. Lett. **27**, 1307 (1991)
48. https://www.rp-photonics.com/midinfraredlasersources
49. J.S. Sanghera, L.B. Shaw, P. Pureza, V.Q. Nguyen, D. Gibson, L. Busse, I.D. Aggarwal, C.M. Florea, F.H. Kung, Nonlinear properties of chalcogenide glass fibers. Int. J. Appl. Glass Sci. **1**, 296 (2010)
50. G. Tao, H. Ebendorff-Heidepriem, A.M. Stolyarov, S. Danto, J.V. Badding, Y. Fink, J. Ballato, A.F. Abouraddy, Infrared fibers. Adv. Opt. Photon. **7**, 379 (2015)
51. A. Jha, B.D.O. Richards, G. Jose, T.T. Fernandez, C.J. Hill, J. Lousteau, P. Joshi, Review on structural, thermal, optical and spectroscopic properties of tellurium oxide based glasses for fibre optic and waveguide applications. Int. Mater. Rev. **57**, 357 (2012)
52. K. Kadono, J. Ceram. Soc. Jpn. **115**, 297 (2007)
53. G.E. Snopatin, V.S. Shiryaev, V.G. Plotnichenka, E.M. Dianov, High-purity chalcogenide glasses for fiber optics. Inorg. Mater. **45**, 1439 (2009)
54. Z. Tang, N.C. Neate, D. Furniss, S. Sujecki, T.M. Benson, A.B. Seddon, Crystallisation behavior of Dy3+-doped selenide glasses. J. Non-Cryst. Solids **357**, 2453 (2011)
55. Z. Tang, V.S. Shiryaev, D. Furniss, L. Sojka, S. Sujecki, T.M. Benson, A.B. Seddon, M.F. Churbanov, Low loss Ge-As-Se chalcogenide glass fiber, fabricated using extruded preform, for mid-infrared photonics, Opt. Mater. Express **5**, 1722 (2015)
56. T. Schweizer, B.N. Samson, R.C. Moore, D.W. Hewak, D.N. Payne, Rare-earth doped chalcogenide glass fibre laser. Electron. Lett. **33**, 414 (1997)
57. S. Cui, R. Chahal, C. Boussard-Pledel, V. Nazabal, J.-L. Doualan, J. Troles, J. Lucas, B. Bureau, From selenium- to tellurium-based glass optical fibers for infrared spectroscopies. Molecules **18**, 5373 (2013)
58. Y.S. Han, J. Heo, Midinfrared emission properties of Pr^{3+} doped chalcogenide glasses at cryogenic temperature. J. Appl. Phys. **93**, 8970 (2003)
59. F. Charpentier, F. Starecki, J.L. Doualan, P. Jvri, P. Camy, J. Troles, S. Belin, B. Bureau, V. Nazabal, Mid-IR luminescence of Dy^{3+} and Pr^{3+} doped $Ga_5Ge_{20}Sb_{10}S(Se)_{65}$ bulk glasses and fibers. Mater. Lett. **101**, 21 (2013)
60. B. Cole, L.B. Shaw, P.C. Pureza, R. Mossadegh, J.S. Sanghera, I.D. Aggarwal, Rare earth doped selenide glass fibers. J. Non-Cryst. Solids **256**, 253 (1999)
61. L. Sojka, Z. Tang, D. Furniss, H. Sakr, A. Oladeji, E. Beres-Pawlik, H. Dantanarayana, E. Faber, A.B. Seddon, T. M. Benson, S. Sujecki, Broadband, mid-infrared emission from Pr^{3+} doped GeAsGaSe chalcogenide fiber, optically clad, Opt. Mater. **36**, 1076 (2014)

62. B.J. Park, H.S. Seo, J.T. Ahn, Y.G. Choi, D.Y. Jeon, W.J. Chung, Mid-infrared (3.5–5.5 μm) spectroscopic properties of Pr^{3+}-doped GeGaSbSe glasses and optical fibers. J. Lumin. **128**, 1617 (2008)
63. M. Ichikawa, Y. Ishikawa, T. Wakasugi, K. Kadono, Mid-infrared emissions from Ho^{3+} in Ga_2S_3-GeS_2-Sb_2S_3 glass. J. Lumin. **132**, 784 (2012)
64. T. Schweizer, B.N. Samsonv, J.R. Hector, W.S. Brocklesby, D.W. Hewak, D.N. Payne, Infrared emission from holmium doped gallium lanthanum sulphide glass, Infrared Phys. Technol. **40**, 329 (1999)
65. T. Schweizer, D.W. Hewak, B.N. Samson, D.N. Payne, Spectroscopy of potential mid-infrared laser transitions in gallium lanthanum sulphide glass. J. Lumin. **72**, 419 (1997)
66. J. Heo, B.S. Yong, Absorption and mid-infrared emission spectroscopy of Dy^{3+} in Ge-As(or Ga)-S glasses. J. Non-Cryst. Solids. **196**, 162 (1996)
67. B.J. Park, H S. Seo, J.T. Ahn, Y.G. Choi, J. Heo, W.J. Chung, Dy^{3+} doped Ge-Ga-Sb-Se glasses and optical fibers for the mid-IR gain media, Ceram. Soc. Jpn. **116**, 1087(2008)
68. M.F. Churbanov, I.V. Scripachev, V.S. Shiryaev, V.G. Plotnichenko, S.V. Smetanin, E.B. Kryukova, Y.N. Pyrkov, B.I. Galagan, Chalcogenide glasses doped with Tb, Dy, and Pr ions. J. Non-Cryst. Solids **326**, 301 (2003)
69. T. Schweizer, B.N. Samson, J.H. Hector, W.S. Brocklesby, D.W. Hewak, D.N. Payne, Infrared emission and ionion interactions in thulium- and terbium-doped gallium lanthanum sulfide glass. J. Opt. Soc. Am. B **16**, 308 (1999)
70. I.D. Aggarwal, J.S. Sanghera, Development and applications of chalcogenide glass optical fibers at NRL. J. Optoelectron. Adv. Mat **4**, 665 (2002)
71. V. Moizan, V. Nazabal, J. Troles, P. Houizot, J-L. Adam, J-L. Doualan, R. Moncorge, F. Smektala, G. Gadret, S. Pitois, G. Canat, Er^{3+}-Doped GeGaSbS glasses for mid-IR fibre laser application: Synthesis and rare earth spectroscopy, Opt. Mater. **31**, 39 (2008)
72. T. Schweizer, D. Brady, D.W. Hewak, Fabrication and spectroscopy of erbium doped gallium lanthanum sulphide glass fibres for mid-infrared laser applications. Opt. Express **1**, 102 (1997)
73. D. Shixun, P. Bo, Z. Pengjun, X. Tiefeng, X. Wang, N. Qiuhua, Z. Xianghua, The near- and mid-infrared emission properties of Tm^{3+}-doped GeGaS-CsI chalcogenide glasses. J. Non-Cryst. Solids **356**, 2424 (2010)
74. G.H. Dieke, H.M. Crosswhite, The spectra of the doubly and triply ionized rare earths. Appl. Opt. **2**, 675 (1963)
75. E. Yahel, O. Hess, A.A. Hardy, Modeling and optimization of high-power $Nd^{3+}-Yb^{3+}$ codoped fiber lasers. IEEE J. Lightwave Technol. **24**, 1601 (2006)
76. C.R. Giles, E. Desurvire, Modeling erbium-doped fiber amplifiers. IEEE J. Lightwave Technol. **9**, 271 (1991)
77. G.C. Valley, Modeling cladding-pumped Er/Yb fiber amplifiers. Opt. Fiber Technol. **7**, 21 (2001)
78. S. Sujecki, *Photonics Modelling and Design* (CRC Press, Boca Raton, 2015)
79. M. Eichhorn, Numerical modeling of Tm-doped double-clad fluoride fiber amplifiers, IEEE J. Quantum Electron. **41**, 1574 (2005)
80. F. Prudenzano, Erbium-doped hole-assisted optical fiber amplifier: Design and optimization, IEEE J. Lightwave Technol., **23**, 330 (2005)
81. J. Liu, H. Hu, C. Shuai, An efficient algorithm based on propagation equations of Tm^{3+}-doped double-clad fiber laser, 2012 Symposium Photonics and Optoelectronics (SOPO), 1–4, 21–23 May (2012)
82. C.A. Evans, Z. Ikonic, B. Richards, P. Harrison, A. Jha, Theoretical modeling of a similar to 2 μm Tm^{3+}-doped tellurite fiber laser: the iInfluence of cross relaxation. IEEE J. Lightwave Technol. **27**, 4026 (2009)
83. C.A. Evans, Z. Ikonic, B. Richards, P. Harrison, A. Jha, A Numerical rate equation modeling of a similar to 2.1 μm - Tm^{3+}/Ho^{3+} co-doped tellurite fiber laser. IEEE J. Lightwave Technol. **27**, 4280 (2009)
84. S.D. Jackson, T.A. King, Theoretical modeling of Tm-doped silica fiber lasers. IEEE J. Lightwave Technol. **17**, 948 (1999)

85. J. Li, L. Gomes, S.D. Jackson, Numerical modeling of holmium-doped fluoride fiber lasers. IEEE J. Quantum Electron. **48**, 596 (2012)
86. S. Sujecki, L. Sojka, E. Beres-Pawlik, Z. Tang, D. Furniss, A.B. Seddon, T.M. Benson, Modelling of a simple Dy^{3+} doped chalcogenide glass fibre laser for mid-infrared light generation. Opt. Quantum Electron **42**, 69 (2010)
87. L. Sojka, Z. Tang, H. Zhu, E. Beres-Pawlik, D. Furniss, A.B. Seddon, T.M. Benson, S. Sujecki, Study of mid-infrared laser action in chalcogenide rare earth doped glass with Dy^{3+}, Pr^{3+} and Tb^{3+}, Opt. Mater. Express **2**, 1632 (2012)
88. R.S. Quimby, L.B. Shaw, J.S. Sanghera, I.D. Aggarwal, Modeling of cascade lasing in Dy:chalcogenide glass fiber laser with efficient output at 4.5 μm. IEEE Photon. Technol. Lett. **20**, 23 (2008)
89. S.D. Jackson, M. Pollnau, J. Li, Diode pumped erbium cascade fiber lasers. IEEE J. Quantum Electron. **47**, 471 (2011)
90. S.D. Jackson, High-power erbium cascade fibre laser. Electron. Lett **45**, 830 (2009)
91. T. Sumiyoshi, H. Sekita, T. Arai, S. Sato, M. Ishihara, M. Kikuchi, High-power continuous-wave 3- and 2-μm cascade Ho^{3+}: ZBLAN fiber laser and its medical applications, J. Sel. Top. Quant. Electron **5**, 936 (1999)
92. J. Kiusalaas, *Numerical Methods In Engineering With MATLAB* (Cambridge University Press, Cambridge, 2010)
93. Y.H. Ja, Using the shooting method to solve boundary-value problems involving nonlinear coupled-wave equations. Opt. Quantum Electron **15**, 529 (1983)
94. S. Sujecki, Stability of steady-state high-power semiconductor laser models, J. Opt. Soc. Am. B **24**, 1053 (2007)
95. X. Liu, B. Lee, A fast and stable method for Raman amplifier propagation equations. Opt. Express **11**, 1452 (2003)
96. L.D. Zohreh, K. Feisa, H.R. Mohammad, An efficient shooting method for fiber amplifiers and lasers. Opt. Laser Technol. **40**, 1041 (2008)
97. Q. Mao, J. Wang, X. Sun, M. Zhang, A theoretical analysis of amplification characteristics of bi-directional erbium-doped fiber amplifiers with single erbium-doped fiber. Opt. Commun. **159**, 149 (1999)

http://www.springer.com/978-3-319-55437-2

Recent Trends in Computational Photonics
Agrawal, A.; Benson, T.; De La Rue, R.; Wurtz, G. (Eds.)
2017, XIX, 395 p. 170 illus., 134 illus. in color.,
Hardcover
ISBN: 978-3-319-55437-2